

X-ray versus infrared selection of distant galaxy clusters: A case study using the XMM-LSS and SpARCS cluster samples

J. P. Willis^{1*}, M. E. Ramos-Ceja², A. Muzzin³, F. Pacaud², H. K. C. Yee⁴, G. Wilson⁵

¹*Department of Physics and Astronomy, University of Victoria, 3800 Finnerty Road, Victoria, BC, V8P 5C2, Canada*

²*Argelander-Institut für Astronomie (AIfA), Universität Bonn, Auf dem Hügel 71. D-53121 Bonn, Germany*

³*Department of Physics and Astronomy, York University, 4700 Keele Street, Toronto, Ontario, M3J 1P3*

⁴*Department of Astronomy and Astrophysics, University of Toronto, 50 St. George Street, Toronto, Ontario M5S 3H4, Canada*

⁵*Department of Physics and Astronomy, University of California-Riverside, 900 University Avenue, Riverside, CA 92521, USA*

Accepted 2018 April 13. Received 2018 April 13; in original form 2017 June 2

ABSTRACT

We present a comparison of two samples of $z > 0.8$ galaxy clusters selected using different wavelength-dependent techniques and examine the physical differences between them. We consider 18 clusters from the X-ray selected XMM-LSS distant cluster survey and 92 clusters from the optical-MIR selected SpARCS cluster survey. Both samples are selected from the same approximately 9 square degree sky area and we examine them using common XMM-Newton, Spitzer-SWIRE and CFHT Legacy Survey data. Clusters from each sample are compared employing aperture measures of X-ray and MIR emission. We divide the SpARCS distant cluster sample into three sub-samples: a) X-ray bright, b) X-ray faint, MIR bright, and c) X-ray faint, MIR faint clusters. We determine that X-ray and MIR selected clusters display very similar surface brightness distributions of galaxy MIR light. In addition, the average location and amplitude of the galaxy red sequence as measured from stacked colour histograms is very similar in the X-ray and MIR-selected samples. The sub-sample of X-ray faint, MIR bright clusters displays a distribution of BCG-barycentre position offsets which extends to higher values than all other samples. This observation indicates that such clusters may exist in a more disturbed state compared to the majority of the distant cluster population sampled by XMM-LSS and SpARCS. This conclusion is supported by stacked X-ray images for the X-ray faint, MIR bright cluster sub-sample that display weak, centrally-concentrated X-ray emission, consistent with a population of growing clusters accreting from an extended envelope of material.

Key words: X-rays: galaxies: clusters.

1 INTRODUCTION

A galaxy cluster is a massive physical structure dominated by a dark matter halo, an intra-cluster medium (ICM) consisting of a hot atmosphere of baryonic gas, and a population of member galaxies. Furthermore, each of the above mass components is in approximate virial equilibrium with the total gravitational potential.

Galaxy clusters represent the most massive structures in the Universe to have achieved this state at the present epoch – with the most extreme examples of such clusters presenting virial masses in excess of $10^{15}M_{\odot}$ (McDonald et al.

2012; Menanteau et al. 2012). Defining a lower mass limit for a galaxy cluster is more problematic. The physical properties of galaxy clusters, such as mass, X-ray luminosity, X-ray temperature, optical richness or velocity dispersion, can be related to each other via simple power laws (Kaiser 1986). Such power law relations appear to be scale free (e.g. Mahdavi & Geller 2001; Anderson et al. 2015), an observation that makes the definition of a minimum galaxy cluster mass an arbitrary statement. However, for the sake of argument, this minimum mass is generally taken to be in the range $\log M/M_{\odot} = 13.5 - 14$ (e.g. Sarazin 1986).

Galaxy clusters are identified by various observational techniques: overdensity searches identify the statistical excess of projected cluster member galaxies in relation to the

* E-mail: jwillis@uvic.ca (JPW)

“background” of non-cluster galaxies along the line-of-sight (e.g. Postman et al. 1996; Gladders & Yee 2000; Rykoff et al. 2014); X-ray searches identify the integrated emission from optically thin bremsstrahlung emission arising from the hot ICM (e.g. Gioia et al. 1990; Böhringer et al. 2001; Clerc et al. 2012); Weak lensing searches identify the integrated shear signal introduced into the shapes of background galaxies by the effect of the cluster mass on local spacetime (e.g. Miyazaki et al. 2002; Wittman et al. 2006; Gavazzi & Soucail 2007); and Sunyaev-Zeld’ovich (SZ) searches identify the apparent decrement in the brightness of the cosmic microwave background (CMB) caused by the inverse Compton scattering of CMB photons by energetic electrons in the ICM (e.g. Staniszewski et al. 2009; Marriage et al. 2011; Reichardt et al. 2013).

Each of these observational techniques is sensitive to a distinct physical component of galaxy clusters: Overdensity searches are sensitive to the integrated star formation history of the cluster; X-ray searches to the projection of the square of the free electron density in the ICM (with a weak dependence upon the ICM temperature); Weak lensing searches to the total projected cluster mass; and SZ searches to the thermal pressure of the free ICM electrons (with small relativistic corrections for the hottest systems).

The question which concerns this paper is how do the physical properties of cluster samples differ depending upon the observational technique used to identify them? Such knowledge is important because it a) permits a consistent comparison between results generated for different cluster samples (e.g. Gilbank et al. 2004; Barkhouse et al. 2006; Rozo & Rykoff 2014; Rossetti et al. 2017) and b) provides a means to relate the results generated for a particular cluster sample to the “true” cluster population (e.g. Borgani et al. 2001; Mantz et al. 2008; Rozo et al. 2010; Planck Collaboration et al. 2014; Jimeno et al. 2017).

At redshifts $z < 0.3$ the comparison between cluster catalogues compiled using different wavebands is mature. Rozo et al. (2014) compare three such low redshift cluster catalogues, selected using optical, X-ray and SZ techniques and demonstrate that each sample can be projected onto a statistically consistent set of common scaling relations.

An alternative approach is to compare cluster catalogues compiled over common sky areas on the basis of individual detections as has been performed by Bergé et al. (2008) using X-ray and weak lensing selected clusters and Starikova et al. (2014) using X-ray, weak lensing and spectroscopically identified clusters. Although to date such comparisons have been limited to small sky areas (4 square degrees or less) and consequently small sample sizes, the conclusions are that clusters that are detected in one waveband but are absent in another can generally be explained by measurement uncertainty and scatter in the relationships between observables and mass.

Two studies which attempt to account for unmatched as well as matched clusters between catalogues have been conducted by Donahue et al. (2002) and Sadibekova et al. (2014), respectively. Each compares an optical and X-ray selected cluster sample typically sensitive to clusters at $z < 1$. Once again, Donahue et al. noted that the relative fraction of optical clusters lacking an X-ray counterpart could be explained by a steep scaling relationship between X-ray and optical cluster luminosity, i.e. $L_X \propto L_{opt}^{3-4}$. In addition, both

studies concluded that the majority of the X-ray clusters lacking an optical counterpart could be attributed to the maximum and minimum effective redshift limitations of the optical cluster selection criteria.

This paper is motivated by the interest in applying a similar comparison to samples of distant galaxy clusters, in this case compiled using data at X-ray and mid-infrared (MIR) wavelengths. This motivation is in part due to the increased potential for cluster-scale astrophysics to influence the observed properties of such clusters and their galaxy populations, e.g. recent star formation (Bayliss et al. 2014; Hayashi et al. 2011; Brodwin et al. 2013; Nantais et al. 2016, 2017), mergers (Nastasi et al. 2011; Lotz et al. 2013), or AGN activity (Galamez et al. 2009; Martini et al. 2013; Ehlert et al. 2015; Alberts et al. 2016). However, because such distant clusters are typically identified at low significance in survey quality data (and thus might be prone to considerable scattering effects on mass-observable relations) we do not compare cluster catalogues compiled at different wavebands via their scaling relations. Instead we apply multiple techniques to determine the extent to which each sample exhibits different physical properties and relate those properties to cluster evolutionary state (e.g. star formation and merger histories).

The structure of the paper is as follows: In Section 2 we describe each distant cluster sample. In Section 3 we describe the available data common to each sample and in Section 4 we use this data to measure fixed aperture brightness values of individual clusters. We present the results of this analysis in Section 5 and draw appropriate conclusions in Section 6. Where necessary we assume a Friedmann-Lemaître-Robertson-Walker cosmological model described by the parameters $\Omega_M = 0.3$, $\Omega_\Lambda = 0.7$, $H_0 = 70 \text{ km s}^{-1} \text{ Mpc}^{-1}$.

2 DISTANT GALAXY CLUSTER SAMPLES

2.1 XMM-LSS

The distant X-ray selected galaxy clusters studied in this paper are taken from Willis et al. (2013). This paper presented a sample of 20 galaxy clusters at $z > 0.8$ selected from an approximately 9 square degree area of the XMM-LSS survey (Pierre et al. 2004). Extended X-ray sources were classified as C1 if they satisfied the criteria `detectionlikelihood > 32`, `extensionlikelihood > 33`, `extension > 5''` and as C2 if they satisfied `extensionlikelihood > 15`, `extension > 5''` (see Pcaud et al. 2006 for further details). In addition, sources were classified as distant clusters if they either possess a known spectroscopic redshift $z > 0.8$ or display a line of sight overdensity of galaxies unlikely to be located at $z < 0.8$. Ten band photometry (*ugrizYJK*[3.6 μm][4.5 μm]) for these latter systems was employed to derive photometric redshifts for bright galaxies deemed to be associated with each extended X-ray source. Candidate clusters were retained in the distant sample if they displayed an overdensity of galaxies consistent with a single location in photometric redshift space at $z_{phot} > 0.8$. Of these 20 clusters, 18 lie within the common footprint of the XMM-LSS/SWIRE/CFHTLS-W1 surveys and were retained for analysis.

2.2 Spitzer Adaptation of the Red Sequence Cluster Survey

The MIR selected distant clusters studied in this paper are taken from the Spitzer Adaptation of the Red Sequence Cluster survey (SpARCS; Muzzin et al. 2009; Wilson et al. 2009). Candidate clusters are identified with significant overdensities in the multiple dimensional space defined by sky position, $z' - 3.6\mu\text{m}$ colour, and $3.6\mu\text{m}$ brightness. Two centroid estimates are provided for each cluster: the first is the sky position of the brightest cluster galaxy (BCG) determined from its location on the cluster red sequence. The second estimate is referred to as the barycentre position and is based upon the mean sky position of all candidate cluster members identified by the red sequence method. We employ both centroid measures in this paper and comment explicitly on how each produces different results. Finally, in addition to the candidate cluster sky position, we also retain the cluster photometric redshift estimate based upon the location of the cluster red sequence in $z' - 3.6\mu\text{m}$ colour.

The SpARCS catalogue located within SWIRE field contains 218 candidate galaxy clusters within the redshift interval $0.1 < z < 1.7$. These correspond to clusters satisfying a richness cut of $N_{red} > 6$, where N_{red} is the number of background-subtracted red-sequence galaxies brighter than $M^*(z) + 1$. The value of $M^*(z)$ is computed from a passive stellar population evolution model formed at $z_f = 4$ (Muzzin et al. 2008). Red-sequence galaxies are defined as those within ± 0.15 magnitudes of the best-fitting $z' - 3.6$ model for each cluster. The threshold $N_{red} > 6$ was set in order to create a sample of clusters suitable for comparison that balanced completeness and purity. From this sample we selected those clusters located within the the combined XMM-LSS/SWIRE/CFHTLS-W1 footprint and lying at $z > 0.8$ for comparison with XMM-LSS.

Although SpARCS employs a richness-based estimator to identify cluster candidates, the inclusion of colour and luminosity information limits the contamination rate arising from projected large-scale structure to 5% at $z < 0.6$ (Gladders & Yee 2000; Gilbank et al. 2018) and to $\sim 15\%$ at $z \sim 1$ (Gilbank et al. 2018). In addition, of the 10 SpARCS clusters observed as part of the Gemini Cluster Astrophysics Spectroscopic Survey (GCLASS; Muzzin et al. 2012), only 1 system, J104737+574137, shows limited evidence of line-of-sight galaxies close to but not at the redshift of the cluster being erroneously assigned cluster membership. The potential also exists for distant clusters to generate multiple detections, especially where each detection is composed of a small number of faint galaxies. With only three pairs of $z > 0.8$ clusters identified within $1'$ of each other on the sky this is not a significant issue. However, in these cases we applied a selection to the SpARCS catalogue to accept the cluster generating the higher signal-to-noise ratio (SNR) detection along the line of sight. These considerations resulted in a sample of 92 clusters for analysis.

2.3 Catalogue matching

An initial means of assessing the commonality of objects appearing in each sample is to match the catalogue positions using a fixed tolerance (e.g. Oguri et al. 2017). We performed such a test using a tolerance of $60''$ (having con-

firmed that this arbitrary threshold does not exclude clusters close to, yet exceeding, this value). The results of the matching procedure are summarised in Table 1 and indicate that 11/12 XMM-LSS clusters at $0.8 < z < 1.4$ are matched to a SpARCS $z > 0.8$ cluster, while at $1.4 < z < 1.7$ the fraction is 1/4. A further two XMM-LSS clusters (IDs 21 and 22) lie beyond the maximum redshift included in the SpARCS red sequence catalogue ($z = 1.7$).

Although the matching fraction for the highest redshift XMM-LSS clusters is low, we note that, in addition to their very high redshift, they possess relatively low masses and display varying red sequence populations (Figure 12 of Willis et al. 2013). It therefore remains plausible that the unmatched, high-redshift XMM-LSS clusters are real clusters that exhibit low stellar mass red sequences such that they do not pass the SpARCS selection criteria.

We performed a second matching analysis, this time comparing SpARCS $z > 0.8$ cluster positions to all detected X-ray sources in the common footprint of the two samples, irrespective of their redshift or morphological classification (i.e. C1, C2, C3 or point source; as described in Pacaud et al. 2006). In this case 33/92 SpARCS $z > 0.8$ clusters were matched within $30''$ to a source in the full XMM-LSS catalogue, rising to 50/92 within a $60''$ matching radius. The majority of X-ray sources contributing to these matches are low-SNR sources of marginally significant extent (C3) in addition to low-SNR point sources (which include unresolved extended sources). However, if we restrict the matching analysis solely to 12 X-ray bright SpARCS clusters (see Section 5.1 for details of X-ray aperture flux measurement), where one would expect a match to the X-ray source catalogue to occur, we find 6/12 and 11/12 matches within 30 and $60''$ respectively. Of these, 3 and 4 respectively are associated with C1 or C2 sources.

Relaxing the restriction on morphological type of X-ray source to which the SpARCS clusters are matched generates a larger fraction of matched objects. This indicates that X-ray sources classified as C1 or C2 within the XMM-LSS survey form a restricted subset of a larger population of gravitationally-bound structures as traced by the SpARCS $z > 0.8$ cluster sample. Furthermore, as will be shown in Section 5.1, the majority of SpARCS $z > 0.8$ clusters display X-ray aperture fluxes which fall significantly below those determined for distant XMM-LSS clusters with the result that the XMM-LSS source detection pipeline fails to recognise them as individual X-ray sources. This is not surprising as the XMM-LSS C1/C2 classification is designed to identify highly significant, extended sources as galaxy clusters in order to construct samples suitable for precision cosmological analyses (following correction for the survey selection function to account for the partial view of the total cluster population).

What is clear however, is that performing a matching analysis will only provide a limited understanding of the physical differences between the XMM-LSS and SpARCS cluster samples. The subsequent analyses in this paper therefore consider the measured properties of individual clusters in each sample at both X-ray and MIR wavelengths as a more direct means of determining the extent and nature of bulk physical differences between the two cluster samples.

Table 1. Matching results between the XMM-LSS and SpARCS $z > 0.8$ cluster samples. The column “ID” refers to the cluster identifier presented in Willis et al. (2013) and the column “XLSSC” lists the short XMM-LSS identifier. The matching code B indicates a cluster match using the BCG centroid and C indicates a match using the barycentre position. The identifier NM indicates that no match was obtained within the $60''$ tolerance. Where $N_{red} \leq 6$, this indicates a match obtained with a cluster lying below the richness cut applied to the SpARCS sample used for analysis in this paper. The X-ray mass values correspond to M_{200c} are taken from Willis et al. (2013) and are computed by applying appropriate scaling relations to the measured X-ray flux and redshift. As discussed in Willis et al. (2013) such mass estimates vary considerably with the assumed scaling relation model and should be taken as indicative, as opposed to exact, values.

ID	Cluster name	XLSSC	Class	Spec. confirmed	XMM-LSS redshift	SpARCS z_{phot}	Match	N_{red}	X-ray mass ($\times 10^{14} M_{\odot}$)
01	XLSS J022400.4-032529	32	C2	Y	0.803	0.98	BC	11.5	$1.21^{+0.25}_{-0.14}$
02	XLSS J022233.8-045803	66	C2	Y	0.833	0.92	BC	8.5	$1.09^{+0.07}_{-0.18}$
03	XLSSU J021832.0-050105	64	C2	Y	0.875	0.98	BC	16.5	$1.26^{+0.08}_{-0.08}$
04	XLSSU J021524.1-034332	67	C1	Y	1.003	1.08	BC	15.8	$2.96^{+0.21}_{-0.19}$
05	XLSS J022253.6-032828	48	C1	Y	1.005	1.13	BC	6.1	$1.45^{+0.19}_{-0.17}$
07	XLSS J022404.1-041330	29	C1	Y	1.050	1.10	BC	11.9	$2.35^{+0.15}_{-0.15}$
08	XLSS J022709.2-041800	5	C1	Y	1.053	1.18*	BC	10.3	$1.17^{+0.07}_{-0.13}$
09	XLSS J022303.3-043621	46	C2	Y	1.213	1.4*	BC	9.2	$0.92^{+0.11}_{-0.15}$
12	XLSSU J021547.7-045027	78	C1	Y	0.953	1.06	BC	4.8	$1.18^{+0.07}_{-0.14}$
13	XLSSU J021859.5-034608		C2	Y	0.979	1.06	BC	5.8	$1.20^{+0.16}_{-0.14}$
14	XLSS J022059.0-043921		C2		$1.11^{+0.29}_{-0.26}$	1.23	C	4.5	$1.06^{+0.14}_{-0.12}$
15	XLSS J022252.3-041647		C2		$1.12^{+0.18}_{-0.17}$	N/A	NM	–	$0.84^{+0.10}_{-0.09}$
16	XLSSU J021712.1-041059		C2		$1.48^{+0.25}_{-0.10}$	N/A	NM	–	$0.97^{+0.12}_{-0.20}$
17	XLSSU J021700.3-034747		C2		$1.54^{+0.30}_{-0.31}$	N/A	NM	–	$0.87^{+0.16}_{-0.14}$
18	XLSSU J022005.5-050824		C2		$1.65^{+0.25}_{-0.26}$	N/A	NM	–	$1.17^{+0.15}_{-0.19}$
20	XLSS J022418.7-043959		C2		$1.67^{+0.20}_{-0.20}$	1.63	BC	4.8	$0.78^{+0.26}_{-0.28}$
21	XLSSU J021744.1-034536	122	C1	Y	1.98	N/A	NM	–	$1.33^{+0.17}_{-0.15}$
22	XLSS J022554.5-045058		C2		$2.24^{+0.26}_{-0.24}$	N/A	NM	–	$0.59^{+0.07}_{-0.09}$

Note: In the two cases marked by an asterisk each has a $z \sim 1.8$ SpARCS cluster providing the closest spatial match; however, the selected clusters are both within the $60''$ matching radius and at similar redshifts.

3 DATA

3.1 X-ray data

X-ray data are obtained from the XMM-LSS survey. The survey has imaged a 11.1 square degree area centered on R.A. = $2^h 22^m$, Dec. = $-4^{\circ} 30'$ with a mosaic of 93 overlapping XMM-Newton pointings (Chiappetti et al. 2013). Each pointing displays a typical exposure time of 10 ks and corresponds to a single observation with the EPIC detectors (MOS1, MOS2 and PN) in full frame imaging mode, spanning a field of view of roughly $30'$ diameter. The effective flux limit for extended sources identified by the C1/C2 surface brightness selection threshold is $\sim 1 \times 10^{-14}$ ergs $s^{-1} cm^{-2}$.

3.2 Spitzer MIR data

Approximately 9 square degrees of the XMM-LSS region has been imaged by the Spitzer space telescope as part of the SWIRE extragalactic survey (Lonsdale et al. 2003). The Spitzer/SWIRE data used in this paper are described in Chiappetti et al. (2013). In particular, we make use of the IRAC channel 1 data corresponding to a photometric bandpass located at $3.6\mu m$. Fluxes for extended sources were measured within the so-called aperture 2^1 and are ex-

pressed in AB magnitudes employing the relation [3.6] = $23.9 - 2.5 \log(f_{\nu}/1\mu Jy)$.

3.3 Optical data

In addition to the X-ray and MIR data described above we also used optical $u^*g'r'i'z'$ photometry obtained from the Canada France Hawaii Telescope Legacy Survey W1 field (CFHTLS-W1; Gwyn 2012). Photometry was computed within an aperture based upon the Kron (1980) radius and quoted on the AB magnitude system. Optical photometry was identified for all sources within the Spitzer MIR catalogue described above. Two independent multi-band catalogues were produced using SExtractor in two-image mode with either the r' - or z' -band image used as the detection band in each case. The construction of separate r' - and z' -selected later permitted a self-consistent examination of the effects of the colour selection of high-redshift cluster galaxies using either $r' - 3.6\mu m$ or $z' - 3.6\mu m$ colours. Optical sources were matched to MIR sources when they are located within a positional tolerance of $< 2''$ with the brightest optical source selected in the case of multiple matches. In the case where a matching optical source was not found, the computed colour of the Spitzer source represents a lower limit based upon the completeness of the optical catalogue in the appropriate

¹ This aperture corresponds to a $1''9$ radius circle with an applied aperture correction which approximates to a total brightness

measure. See Section 4.11.2 of the IRAC instrument handbook or <http://irsa.ipac.caltech.edu/data/SPITZER/docs/irac/iracinstrumenthandbook>

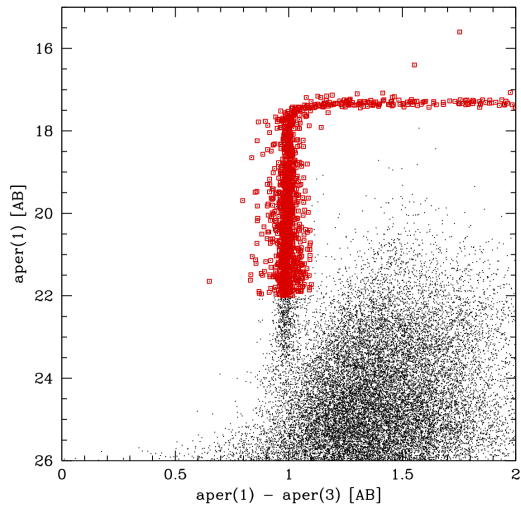


Figure 1. An example of star/galaxy separation applied to a particular r' -band image of the CFHTLS data set (“Field A”). The red points indicate sources identified as stars. Star-galaxy separation is performed for sources satisfying $\text{aper}(1) < 22$ AB. No separation is performed fainter than this threshold.

band. Finally, star-galaxy separation was performed upon the matched catalogue in the appropriate optical detection band using the distribution of sources on the plane defined by $\text{aper}(1) - \text{aper}(3)$ versus $\text{aper}(1)$ where $\text{aper}(n)$ is the magnitude measured in an aperture of diameter equal to n arcseconds (these quantities represent measures of source extent and brightness respectively; Figure 1).

4 FIXED APERTURE BRIGHTNESS MEASURES

Given the two cluster samples described above and a common X-ray, optical and MIR data set, it is possible to measure X-ray and MIR brightness measures for all clusters employing a simple, consistent approach.

The cluster signal in each waveband was measured in a circular aperture of fixed radius equal to $1'$ centered on the X-ray position for XMM-LSS clusters and either the BCG or the barycentre position for SpARCS clusters. This approach was selected to measure the cluster signal in as robust a manner as possible and using the fewest assumptions regarding the properties of individual clusters. For example, this approach requires only the sky position of each cluster and thus lends itself well to comparing cluster samples drawn from a variety of selection approaches.

Application of a circular aperture is the simplest response to the lack of data on the shapes of distant clusters. Furthermore, application of a fixed angular radius offers a number of advantages: the background applied to correct the

line-of-sight signal from each cluster is uniform across the sample. As the line-of-sight signal from each cluster is often background dominated, this generates consistent and comparable uncertainties across the sample of measurements.

In addition, although one could choose to apply an aperture of fixed physical radius in the rest frame of each cluster it should be noted that, over the redshift interval $0.8 < z < 2$ and within the assumed cosmological model, the angular diameter distance (required to convert from angular to physical radius) varies by approximately $\pm 5\%$ about the fiducial redshift $z = 1$.

4.1 X-ray aperture photometry

The X-ray brightness measurement from a galaxy cluster is sensitive to the emission from gravitationally confined gas at the virial temperature of the cluster gravitational potential. The X-ray brightness of a cluster is primarily a measure of the (square of) the baryonic gas mass with a slowly varying dependence upon the cluster gas temperature.

We implemented a Bayesian approach for calculating X-ray aperture photometry. The method is an adaptation from the approach taken by van Dyk et al. (2001) and Park et al. (2006). In the following we explain our procedure.

Net source counts are computed from independent source and background apertures areas. Sky areas associated with non-extended source detections (i.e. non-C1 or C2) were masked from this process to remove any possible contribution from X-ray Active Galactic Nuclei (AGN). We assume that C counts are measured in a source aperture of area A_s , and B counts are measured in a background aperture of area A_b . The observed counts are generated via a Poisson process, i.e.,

$$C \sim \text{Poisson}(f(s + b)), \quad (1)$$

$$B \sim \text{Poisson}(rgb), \quad (2)$$

where C is given by the sum of counts due to the source, s , and the background, b . The symbols $f = 1/T_s$ and $g = 1/T_b$ are factors that convert the net counts to count-rates given the average exposure time in A_s and A_b . The quantity r is an area correction factor given by $r = A_b/A_s$. We determine s from its posterior probability density marginalized over the background,

$$p(s|CB) = \int db p(sb|CB). \quad (3)$$

Via Bayes' theorem, the joint posterior probability of s and b can be rewritten as

$$p(sb|CB) = \frac{p(s)p(b)p(C|sb)p(B|b)}{\int \int db ds p(s)p(b)p(C|sb)p(B|b)}. \quad (4)$$

$p(C|sb)$ and $p(B|b)$ are Poisson distributions, and $p(s)$ and $p(b)$ are generalized γ -priors. Further details in the final analytical derivation of $p(s|CB)$ can be found in Appendix A2 of Park et al. (2006). In our work we assume non-informative priors, given as the result

$$p(s|CB) = A^{-1} \times B, \quad (5)$$

where

$$A = \left[\sum_{j=0}^C \frac{1}{\Gamma(j+1)\Gamma(C-j+1)} \frac{\Gamma(C+B+1-j) \Gamma(1+j)}{(f+gr)^{C+B+1-j} f^{1+j}} \right] \quad (6)$$

and

$$B = \sum_{j=0}^C \frac{1}{\Gamma(j+1)\Gamma(C-j+1)} \frac{\Gamma(C+B+1-j)}{(f+gr)^{C+B+1-j}} s^j e^{-fs}. \quad (7)$$

The value of s is obtained from the mode of $p(s|CB)$ distribution, and the confidence levels are determined by numerically integrating $p(s|CB)$ until the desired confidence level is reached. In this way, if the mode of $p(s|CB)$ is equal to 0, one can still provide upper limit for s .

We applied the above approach to the clusters in the sample to obtain their X-ray aperture photometry. Apertures of $1'$ radius are used and are located on the cluster centroid. We have two ways to obtain the background counts depending on the cluster position in the XMM pointing:

- If the cluster centroid is close ($<2'$) to the pointing center, the background aperture is defined as an annulus centered on the cluster position. The annulus has a width of $1'$, and is $1'$ away from the source aperture to avoid contamination from the cluster.
- If the cluster centroid is far ($>2'$) from the pointing center, the background aperture is an annulus encompassing the cluster aperture and at similar off-axis angle. A quadrant of 45 degrees (centered on the cluster) is excluded from the background measurement to avoid residual cluster contamination.

This approach accounts for the radial variation of the XMM background. The procedure is applied separately to each XMM-Newton EPIC detector, obtaining three different count-rate posterior probability density distributions for each cluster. We then convert each count-rate distribution into a flux posterior probability density, $p(f)$, through an energy conversion factor (ECF). This factor is calculated using XSPEC (Arnaud 1996) and an APEC emission model with $z = 1$, $T = 2$ keV, $N_H = 2.6 \times 10^{20}$ cm², $Ab = 0.3$, and standard on-axis EPIC response matrices. The ECF scales the flux of the three EPIC detectors to a common sensitivity. The final flux posterior probability density, $p(f_X)$, for a given cluster is obtained by multiplying the individual flux distributions of the different EPIC detectors:

$$p(f_X) = \prod_{i=1}^3 p(f_i), \quad (8)$$

where i refers to the three EPIC detectors. The final X-ray flux is obtained from the mode of $p(f_X)$, together with its corresponding 68% confidence levels.

4.2 Spitzer MIR aperture photometry

The Spitzer MIR brightness measurement for a galaxy cluster is computed as the summed stellar $3.6\mu\text{m}$ brightness of individual galaxies identified as cluster members. To determine membership we applied a colour cut to the optical-MIR source catalogue to identify candidate $z > 0.8$ galaxies (e.g. Muzzin et al. 2008).

We investigated the application of two cuts designed to select $z > 0.8$ passive galaxies, namely $r' - 3.6\mu\text{m} > 3.4$ and $z' - 3.6\mu\text{m} > 1.3$. The MIR fluxes of those galaxies that satisfy these colour cuts and lie within $1'$ of the cluster centroid are then summed to provide a two separate $3.6\mu\text{m}$ flux

measurements per cluster. Much of the analysis in the subsequent sections was repeated using aperture fluxes and luminosities computed using either the $r' - 3.6\mu\text{m}$ and $z' - 3.6\mu\text{m}$ cuts. However, at this point we note that all of the analysis which follows generated similar results and conclusions irrespective of which colour cut was considered. The use of two colour cuts therefore provided useful a consistency check but, in the interests of brevity, we only present results derived using the $r' - 3.6\mu\text{m}$ colour cut.

Each aperture measurement was corrected for unassociated galaxies along the line of sight employing a sample of 5000 randomly placed $1'$ apertures located within the common survey footprint and using the same photometric thresholds as applied to the cluster samples. Although most non-cluster galaxies will lie in the foreground of a distant cluster, for simplicity we refer to these randomly placed apertures as “the background”. We rejected background apertures which lay within $2'$ of any SpARCS cluster to retain a sample of 4667 apertures for analysis. The distribution of background aperture flux measurements was modelled as a Gaussian function modified by a shallow power law to describe a slight skewness of the observed distribution toward higher background values. The source flux in each cluster aperture was then computed as the maximum value of the posterior distribution of the cluster aperture flux (source plus background) minus the background model with the prior that the source flux $s \geq 0$. The error on each cluster flux measurement is computed from the interval of the above posterior distribution per cluster which contains 68% of the distribution.

5 RESULTS

5.1 X-ray versus MIR flux and luminosity measures

Figure 2 compares the cluster $3.6\mu\text{m}$ summed aperture flux to the X-ray aperture flux measured for 18 XMM-LSS and 92 SpARCS $z > 0.8$ clusters. This comparison uses the $r' - 3.6\mu\text{m} > 3.4$ colour cut and employs the BCG position of each SpARCS cluster.

Two initial impressions are apparent from this comparison. Firstly, there is a broad correlation in luminosity defined by X-ray faint, MIR faint ranging to X-ray bright, MIR bright clusters. We do not attempt to quantify this trend in the current study as the measurement approach taken is deliberately simple and is designed to provide a robust comparison between clusters of widely different properties. Secondly, in contrast to this broadly defined correlation between X-ray gas emission and stellar emission within both cluster samples, there exist a number of MIR selected clusters which, although they are among the brightest MIR sources in either sample, appear to be relatively deficient in measured X-ray aperture flux or luminosity. Some caution is required: there is much scatter in the measured distributions displayed in Figure 2 and the apparently MIR bright, X-ray faint clusters mentioned above do not represent significant outliers. However, the distributions displayed in Figure 2 are sufficiently interesting to investigate whether splitting the SpARCS clusters into sub-samples based upon their measured aperture fluxes identifies physically distinct clusters.

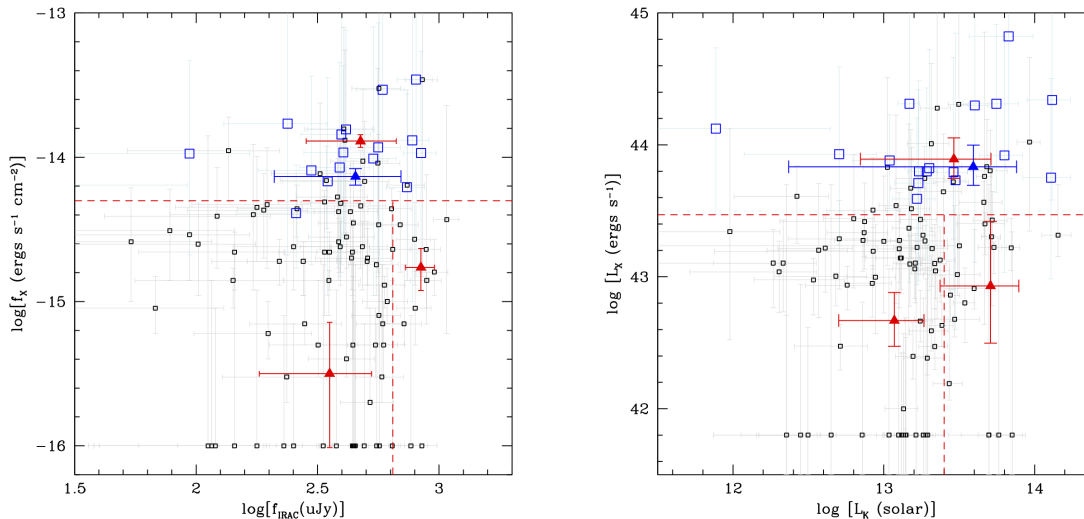


Figure 2. A comparison of X-ray and MIR $1'$ aperture brightness values for XMM-LSS (blue squares) and SpARCS (black squares) clusters. This comparison uses the $r - 3.6\mu\text{m} > 3.4$ colour cut and employs the BCG position of each SpARCS cluster. Error bars indicate the 68% interval of the posterior background subtracted flux distribution for each source. The red dashed lines indicate the selection cuts applied to generate sub-samples of the SpARCS cluster for further analysis. Left: Comparison by flux. SpARCS clusters with zero measured X-ray flux are marked at $\log f_X = -16$ for clarity. The solid triangles indicate the fluxes measured for the stacked cluster samples (see Section 5.5); red indicates SpARCS and blue indicates XMM-LSS clusters. Right: Comparison by luminosity. SpARCS clusters with zero measured X-ray luminosity are marked at $\log L_X = -41.8$ for clarity. See text for further details.

In the following sections we compare the physical properties of the XMM-LSS sample to three sub-samples based upon the distribution of the SpARCS clusters on the X-ray/MIR plane displayed in Figure 2 – the aim being to determine if each sub-sample displays quantifiable physical differences. We define X-ray bright MIR selected clusters as those displaying $f_X \geq 0.5 \times 10^{-14} \text{ ergs s}^{-1} \text{ cm}^{-2}$. We further split X-ray faint ($f_X < 0.5 \times 10^{-14} \text{ ergs s}^{-1} \text{ cm}^{-2}$) MIR selected clusters into those which are MIR bright ($f_{3.6\mu\text{m}} \geq 650 \mu\text{Jy}$) and faint ($f_{3.6\mu\text{m}} < 650 \mu\text{Jy}$). These thresholds are defined arbitrarily yet identify the broad trends present in the above diagrams, the most important of which appears to be that a significant fraction of the brightest SpARCSs cluster, whether defined by MIR flux or luminosity, appear deficient in X-ray emission. Though defined in this manner it is important to note that the conclusions presented in this paper are relatively insensitive to the exact choice of threshold values applied. The final numbers of clusters present in each sample are as follows: XMM-LSS, 18; SpARCS X-ray bright, 12; SpARCS X-ray faint, MIR bright, 10; SpARCS X-ray faint, MIR faint, 70.

There exists the concern that the X-ray faint, MIR bright sub-sample of SpARCS clusters could be due to intrinsically X-ray faint, MIR faint clusters boosted by high local background values that are under-subtracted by the modal value of the global background applied in Section 4.2. To investigate this issue we computed local backgrounds

about each SpARCS cluster using a circular annulus at a fixed radial distance from the cluster centroid. Applying a background annulus with inner and outer radii respectively 5 and 6 arcminutes from each cluster centroid generated a set of background values distributed symmetrically about the global background computed in Section 4.2 with no evidence of clusters with high MIR aperture flux measurements displaying enhanced local background values. Identification of X-ray faint, MIR bright clusters in Figure 2 is therefore not influenced by the application of a global background correction to MIR cluster aperture fluxes.

It is furthermore unlikely that the non-cluster masking procedure applied to the computation of X-ray aperture fluxes results in the exclusion of bona-fide cluster flux from the aperture measurement. As mentioned previously, XMM-LSS pipeline detections corresponding to non-C1/C2 sources were masked from the aperture measurement. An alternative masking procedure was tested, this time excluding source areas corresponding only to point sources classified as P1 (high significance, low extension), with little or no qualitative difference in the results presented above.

We also compare the X-ray and MIR brightness measures of each cluster sample in terms of their luminosity using the measured redshift for each cluster and the assumed cosmological model to convert the measured aperture flux in either the X-ray or IRAC1 band respectively to a rest-frame [0.5-2] keV X-ray and K -band stellar luminosity.

In addition to the luminosity distance to each source, the correction to luminosity requires the application of a k -correction. For the X-ray brightness this correction is computed using the same $T = 2$ keV plasma model used to convert count rates to flux. In the MIR we employ a k -correction derived from a 1 Gyr, solar metallicity burst of star formation which evolves passively from a formation redshift $z_f = 10$. This model is taken from Willis et al. (2013) and matches the red sequence evolution of the XMM-LSS distant cluster sample. Furthermore, as demonstrated by van der Burg et al. (2014), the stellar mass in SpARCS distant clusters is dominated by M^* galaxies located on the red sequence. The evolving spectrum was realised using the GALAXEV 2003 stellar population synthesis code (Bruzual & Charlot 2003).

Computing the MIR luminosity of a galaxy cluster within a spatial aperture effectively involves integrating the cluster galaxy luminosity function (LF) down to a sensitivity limit which itself may be expected to be a function of redshift. In order to determine whether this is likely to be an important bias in the aperture luminosity values computed for this paper we performed the following analysis: taking the $3.6\mu\text{m}$ flux limit of the optical-MIR catalogue as $3.7 \mu\text{Jy}$ we computed the corresponding K -band luminosity of a galaxy with this flux over the redshift interval $0.8 < z < 1.6$ (the extent of the SpARCS sample). We next considered this luminosity as the limiting value as a function of redshift to which we integrated the K -band cluster galaxy LF presented by De Propriis et al. (2007). The relative change in the value of this integral over a function of redshift indicates the expected effect on the measured aperture luminosity values. This LF correction factor varies with respect to a fiducial value at $z = 1$ by $\pm 5\%$ over the interval $0.8 < z < 1.2$ (which includes over 85% of the SpARCS clusters) and by 20% at the maximal redshift $z = 1.6$ of the SpARCS catalogue. These correction factors are applied to the aperture luminosity measurements shown in Figure 2 yet we note that they are small compared to the measurement errors (which are dominated by background variations).

We apply X-ray and MIR brightness cuts to the aperture luminosity measurements in an analogous manner to those applied to the flux data. Recall that the XMM-LSS and SpARCS samples contain 18 and 92 clusters respectively. We define X-ray luminous MIR selected clusters as those displaying $L_X \geq 0.3 \times 10^{44} \text{ ergs s}^{-1} \text{ cm}^{-2}$. We further split X-ray faint ($L_X < 0.3 \times 10^{44} \text{ ergs s}^{-1} \text{ cm}^{-2}$) MIR selected clusters into those which are IR luminous ($L_K \geq 2.5 \times 10^{13} L_\odot$) and faint ($L_K < 2.5 \times 10^{13} L_\odot$). The final numbers of clusters present in each sample are as follows: XMM-LSS, 18; SpARCS X-ray bright, 17; SpARCS X-ray faint, IR bright, 16; SpARCS X-ray faint, IR faint, 59. There is considerable overlap between cluster sub-samples defined by flux and luminosity. For example of the 12 high flux SpARCS clusters defined using the BCG position, 11 are present in the luminosity defined sample. Of the 10 X-ray faint, MIR bright clusters defined by flux, 7 are present in the corresponding luminosity defined sample.

Figure 3 shows the cumulative fraction distribution in positional offset (BCG-barycentre position) and redshift of each cluster sub-sample selected either on the basis of aperture flux or aperture luminosity measurements. A number of trends are apparent, notably that the X-ray faint, MIR faint

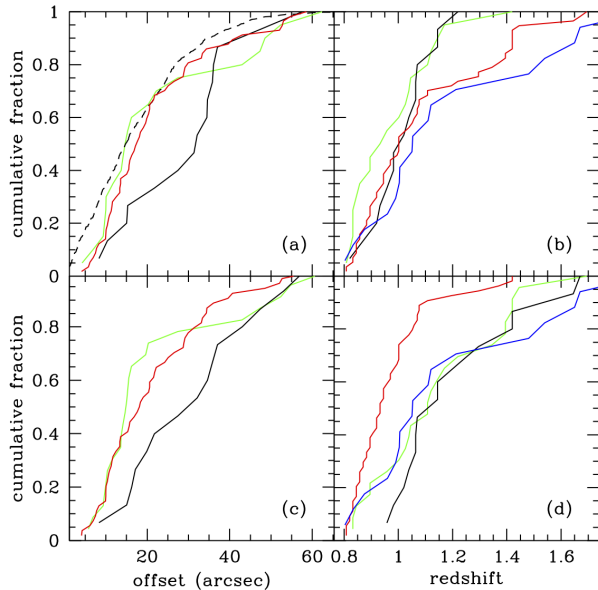


Figure 3. The cumulative fraction distribution in both offset (BCG-barycentre position) and redshift of each cluster sub-sample: XMM-LSS (blue), X-ray bright SpARCS (green), X-ray faint MIR faint SpARCS (red), X-ray faint, MIR bright (black). Panels a) offset distribution of cluster sub-samples selected on the basis of aperture flux measurements, b) redshift distribution of cluster sub-samples selected on the aperture flux measurements. Panels c) and d) follow panels a) and b) for cluster sub-samples selected on the basis of aperture luminosity measurements. The black dashed line in panel (a) indicates the BCG-barycentre offset distribution expected from a $22''$ 1D Gaussian random error in the barycentre centroid values (see Section 5.2 for more details).

cluster sub-sample is composed of distant, i.e. higher redshift, intrinsically luminous clusters when selected by aperture flux and nearby, i.e. lower redshift, intrinsically faint clusters when selected by luminosity. In each case the sub-sample of X-ray faint, MIR bright clusters, whether selected by flux or luminosity, displays a distribution of position offsets between the BCG and barycentre position dominated by higher values than other cluster sub-samples. Furthermore, this conclusion holds whether the selection of X-ray faint, MIR bright clusters is performed using either $r' - 3.6$ or $z' - 3.6$ colour and either BCG or barycentre centroids for aperture measurements.

5.2 Cumulative MIR angular surface brightness profiles

The average MIR angular surface brightness distribution within each cluster sub-sample was computed using the relation

$$\mu(r_i) = \frac{\sum_{i=1}^N f_{3.6\mu m, i}}{4\pi r_N^2}, \quad (9)$$

where $f_{3.6\mu m, i}$ and r_i are respectively the $3.6\mu m$ flux and angular separation from the appropriate cluster centroid of a list of N galaxies within each cluster sub-sample ordered by increasing r_i . Once again, the X-ray centroid is used as the reference position for XMM-LSS clusters and the BCG position is used for SpARCS. Note that to avoid infinite values of central surface brightness in the case where the BCG position is used we apply a softening radius to Equation 9 of the form $r_N = r_N + r_S$ with r_S equal to $1''.8$. We also note that the above cumulative formalism generates qualitatively the same results as a differential approach which computes the surface brightness in radial bins about each cluster centre yet avoids an arbitrary choice of radial bins. The surface brightness expressed in terms of rest-frame K -band luminosity per unit area can also be computed in a straightforward manner by replacing the flux of each colour-selected candidate cluster galaxy along the line-of-sight with the luminosity computed with the appropriate distance modulus and k -correction discussed in Section 5.1. Figure 4 displays the resulting surface flux and luminosity profiles for each cluster sub-sample. Taken together, the figures indicate that both X-ray selected and either X-ray bright or MIR-bright colour-selected clusters display similar projected distributions of galaxy light respectively about either the X-ray or BCG location. X-ray faint, MIR-faint SpARCS clusters display similar profiles yet with lower normalisation. Note that this procedure does not account for the background of non-cluster galaxies along the line-of-sight. However, each distribution tends to an asymptotic background value at large radius. In the left panel of Figure 4 one notes that all distant cluster projected surface brightness distributions are clearly different from the average distribution of background galaxies within a 1 arcminute radius aperture.

We repeated the above analysis using the barycentre position of each SpARCS cluster instead of the BCG location. The results are plotted in Figure 5 and indicate that each sub-sample of SpARCS clusters displays a central deficit of light compared to the analysis using the BCG location.

We investigated whether this apparent deficit was due to large errors in the barycentre centroid values relative to the BCG positions measured for the SpARCS clusters. Such centroid errors, based upon the average position of candidate cluster members, are a persistent feature of galaxy overdensity cluster finding algorithms (e.g. Lin, Mohr & Stanford 2004; Rozo & Rykoff 2014; Oguri et al. 2017). We restricted our analysis to the SpARCS X-ray bright clusters assuming that these represent bona-fide clusters where the BCG location is close to the true centroid of each cluster. We applied a random Gaussian offset to the measured BCG right ascension and declination of each cluster and recomputed the stacked surface brightness profile as described above. We repeated this process N times to generate an ensemble of surface brightness distributions at each specified offset (Figure 6).

The results indicate that the SpARCS X-ray bright barycentre surface brightness distribution is consistent with that generated employing BCG positions convolved with a 1D centroid error in R.A. and dec. of $\sigma = 15''$, corresponding

to an error of $22''$ in radius. Figure 3 (panel (a)) indicates that this error model describes a large component, though not all, of the observed distribution of BCG-barycentre offset values for the SpARCS X-ray bright (and X-ray faint, MIR faint) sub-samples.

The X-ray faint, MIR bright SpARCS clusters display a distribution of centroid offsets in excess of this centroid error model and likely indicates an additional, intrinsic offset distribution. In studies at lower redshifts, large positional offsets between the BCG location and other measures of cluster centroid (e.g. X-ray location or average member galaxy location) are often taken as an indicator of a cluster displaying the effects of incomplete virial relaxation (e.g. Sanderson, Edge & Smith 2009; Lavoie et al. 2016).

It may be that the location of X-ray faint, MIR bright SpARCS clusters on the X-ray versus MIR aperture brightness diagrams shown in Section 5.1 is explained by such disturbance/virialisation arguments. However, further evidence must be considered before reaching a conclusion, namely performing a visual assessment of individual clusters in each sub-sample and considering stacked, two-dimensional X-ray images of each sub-sample.

5.3 Visual assessment

It is sensible to determine whether the trends in radial surface brightness presented in Section 5.2 are supported by a visual assessment of individual clusters in each sub-sample. Figures 7, 8, 9 and 10 display Spitzer/IRAC $3.6\mu m$ images of clusters drawn from the XMM-LSS, SpARCS X-ray bright, SpARCS X-ray faint, MIR bright and SpARCS X-ray faint, MIR faint samples respectively.

Although a visual assessment can only deliver qualitative information, it is clear that the images of clusters in each sub-sample support the surface brightness trends presented in Section 5.2 with both the XMM-LSS and SpARCS clusters appearing as centrally concentrated systems of galaxies.

The sub-sample of SpARCS X-ray faint, MIR faint clusters presents a range of appearances, largely consistent with their low MIR aperture fluxes. There is some evidence for central concentrations of galaxies in the $3.6\mu m$ images. However, there are also numerous examples, particularly at higher redshift, of images sparsely populated by galaxies where no conclusive statement can be made on the basis of visual inspection.

5.4 Stacked colour magnitude diagrams

The creation of stacked colour magnitude diagrams for each cluster sub-sample provides an opportunity to assess whether each represents a population of galaxies drawn from a narrow range of star formation histories. In particular the presence, location and width of the characteristic cluster red sequence provides measure of the average evolved galaxy population within each cluster sub-sample.

Photometry corresponding to $3.6\mu m$ magnitudes and $r' - 3.6\mu m$ colours for galaxies located within $1'$ of each cluster centroid were obtained. Photometry for different clusters in each sub-sample were each transformed from the catalogue redshift of each cluster to a common reference of $z = 1$ by applying an appropriate k - and distance modulus correction as discussed in Section 5.1.

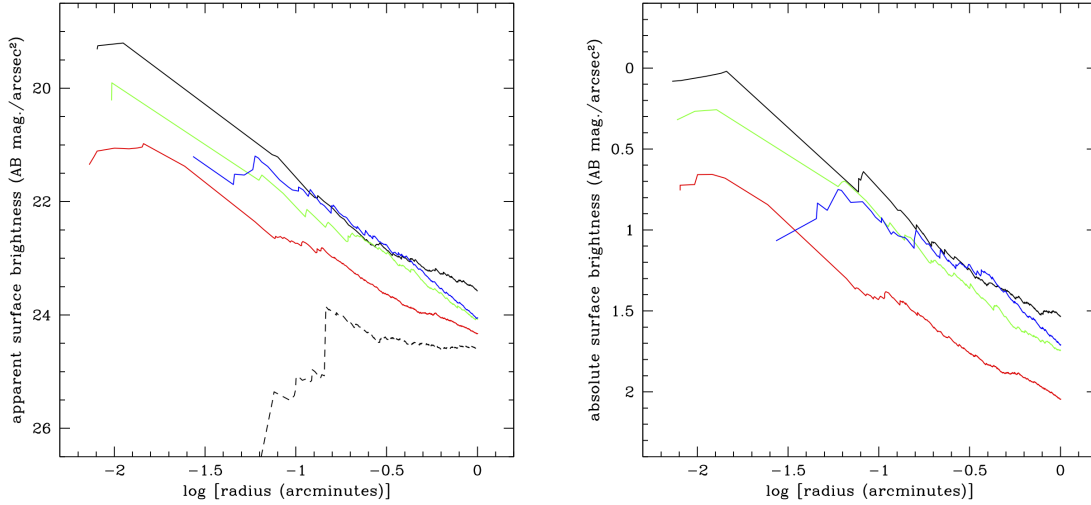


Figure 4. The cumulative angular MIR surface brightness distribution of each cluster sub-sample: XMM-LSS (blue), X-ray bright SpARCS (green), X-ray faint MIR faint SpARCS (red), X-ray faint, MIR bright (black). Left panel: Surface brightness computed using flux. The black dashed line indicates the average cumulative surface brightness distribution computed from 100 randomly placed apertures. Right panel: Surface brightness computed using luminosity. Note that no background is displayed in this panel as it is not possible to apply a conversion between flux and luminosity given the unknown redshift distribution of the background galaxies.

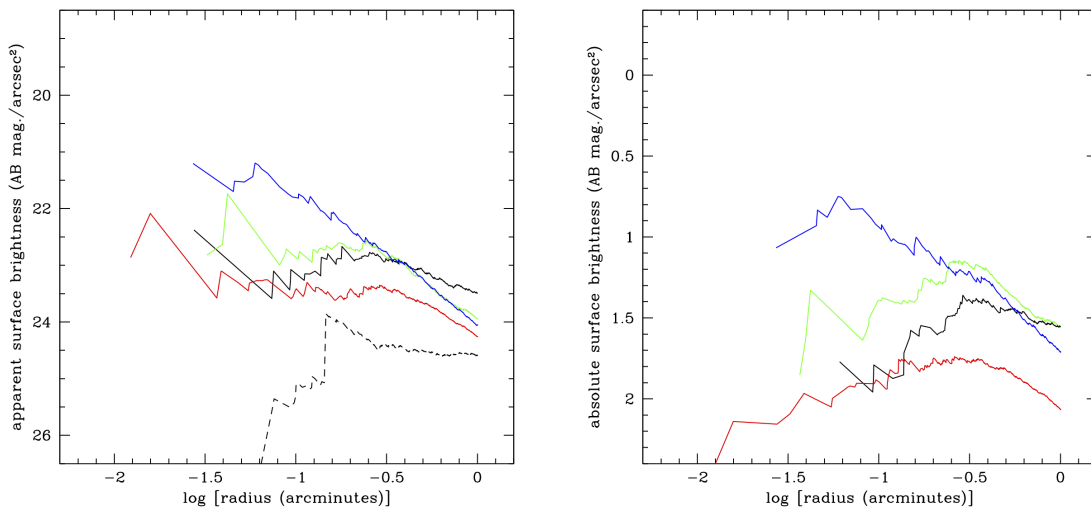


Figure 5. The cumulative angular MIR surface brightness distribution of each cluster sub-sample: XMM-LSS (blue), X-ray bright SpARCS (green), X-ray faint MIR faint SpARCS (red), X-ray faint, MIR bright (black). Centroids for SpARCS clusters employ the barycentre position. Note that the axis scale employed in this figures is the same as Figure 4.

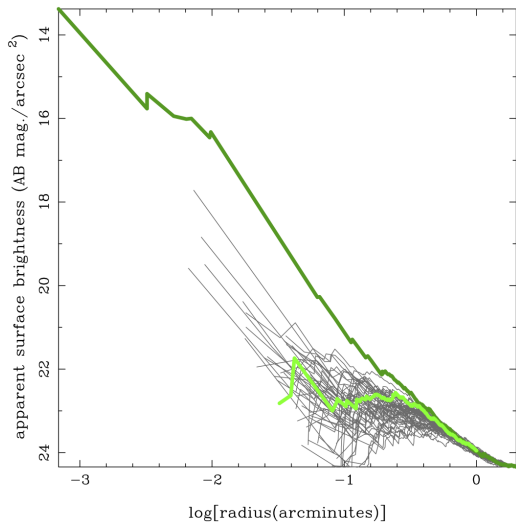


Figure 6. A detailed comparison of the cumulative surface brightness distributions of the SpARCS X-ray bright clusters employing BCG (dark green) and barycentre (light green) centroid values. The set of grey lines indicate 50 simulations of the stacked surface brightness calculation in which a random Gaussian offset of $\sigma = 15''$ is applied to each cluster BCG R.A. and dec. centroid prior to stacking.

Figure 11 isolates the red sequence distribution by collapsing the colour-magnitude plane along the $3.6\mu\text{m}$ magnitude axis to create a colour histogram for each cluster sub-sample. All sources displaying a redshift-corrected magnitude $[3.6\mu\text{m}] < 21$ AB are co-added following this method. Despite the changing normalisation of each sub-sample as one proceeds from XMM-LSS clusters to SpARCS X-ray bright and finally to SpARCS X-ray faint, MIR faint clusters it is clear that each displays a similar red sequence distribution, i.e. each contains a red galaxy population of approximately similar absolute age and scatter.

The comparison indicates that the typical number of red sequence galaxies located in XMM-LSS clusters is comparable to that found in the X-ray faint, MIR faint sub-sample of SpARCS clusters, echoing earlier comparisons between distant X-ray and IR-selected clusters (Foltz et al. 2015). SpARCS clusters labelled as X-ray bright and X-ray faint, MIR bright each display more populous red sequence distributions, marginally in the case of X-ray bright systems more significantly for X-ray faint, MIR bright clusters (though omitted for clarity, the typical Poisson error for each data point in Figure 11 is approximately 0.25-0.3).

5.5 Stacked X-ray images

The creation of stacked X-ray images for each cluster sub-sample permits the average X-ray emission properties of each to be discussed. Furthermore, the low noise properties of stacked images in particular permits a sensitive test of the average emission from the SpARCS X-ray faint sub-samples to be investigated.

We examine stacked images of the cluster sub-samples

using the data from the XMM-LSS survey. In brief, for each sub-sample and for each EPIC detector we follow this procedure:

- (i) Extract a $2'$ radius EPIC image and corresponding exposure map for each cluster in the $[0.5-2]$ keV band.
- (ii) Create a background map for each field by fitting a two component model to source masked EPIC images. In this way, the effects of spatial variation in the background are taken into account.
- (iii) Mask out all point sources in each image, exposure and background maps. Point source locations are obtained from the XMM-LSS pipeline.
- (iv) Sum each of the EPIC images to produce a stacked image. Also sum each of the individual exposure and background maps. In this step, the MOS exposure maps are weighted according to the MOS/PN response ratio. The relative sensitivity of the MOS and PN detectors is calculated with XSPEC using standard on-axis PN and MOS response matrices.

The final count-rate image is obtained by subtracting the stacked background map from the stacked photon image and dividing by the stacked exposure map. Figures 12 and 13 shows the final images for each sub-sample stacked by either flux or luminosity. As a test of our flux stacking procedure we also analyzed a set of 100 randomly selected positions from the XMM-LSS region in an identical way as the real cluster positions. Luminosity stacks are created from flux stacks employing an energy conversion factor based upon the mean redshift of each sub-sample.

Highly significant X-ray emission is seen in both the XMM-LSS and X-ray bright SpARCS sub-samples when compared to the image created by combining 100 random locations. Weaker emission is also detected in the stacked image corresponding to the X-ray faint, MIR bright sub-sample. It is apparent that the spatial distribution of X-ray emission in the SpARCS sub-samples is associated more closely with the cluster BCG position compared to the barycentre position. This is indicated visually in the stacks for the X-ray bright and X-ray faint, MIR bright sub-sample where more compact, centrally-peaked X-ray emission is generated when stacking on the BCG position. The stacked image for the X-ray faint, MIR faint SpARCS sub-sample displays only marginal X-ray emission in excess of random when stacking on the BCG position – a result consistent with the low overall aperture X-ray flux measurements for this sub-sample. Stacking in luminosity largely confirms these trends yet with additional substructure present in the stacked images. This is attributed to individual distant sources in each sub-sample for which a large correction is obtained when converting pixel values from count rate to luminosity.

The visual trends noted in the stacked images are reinforced by inspection of the angular X-ray surface brightness distributions in each cluster sub-sample shown in Figures 14 and 15. The results confirm that the X-ray emission in each SpARCS sub-sample is consistent with being centred on the BCG and that the X-ray faint, MIR bright sub-sample displays weak yet significant extended X-ray emission. The surface brightness distributions computed using barycentre centroids are suppressed relative to those computed using

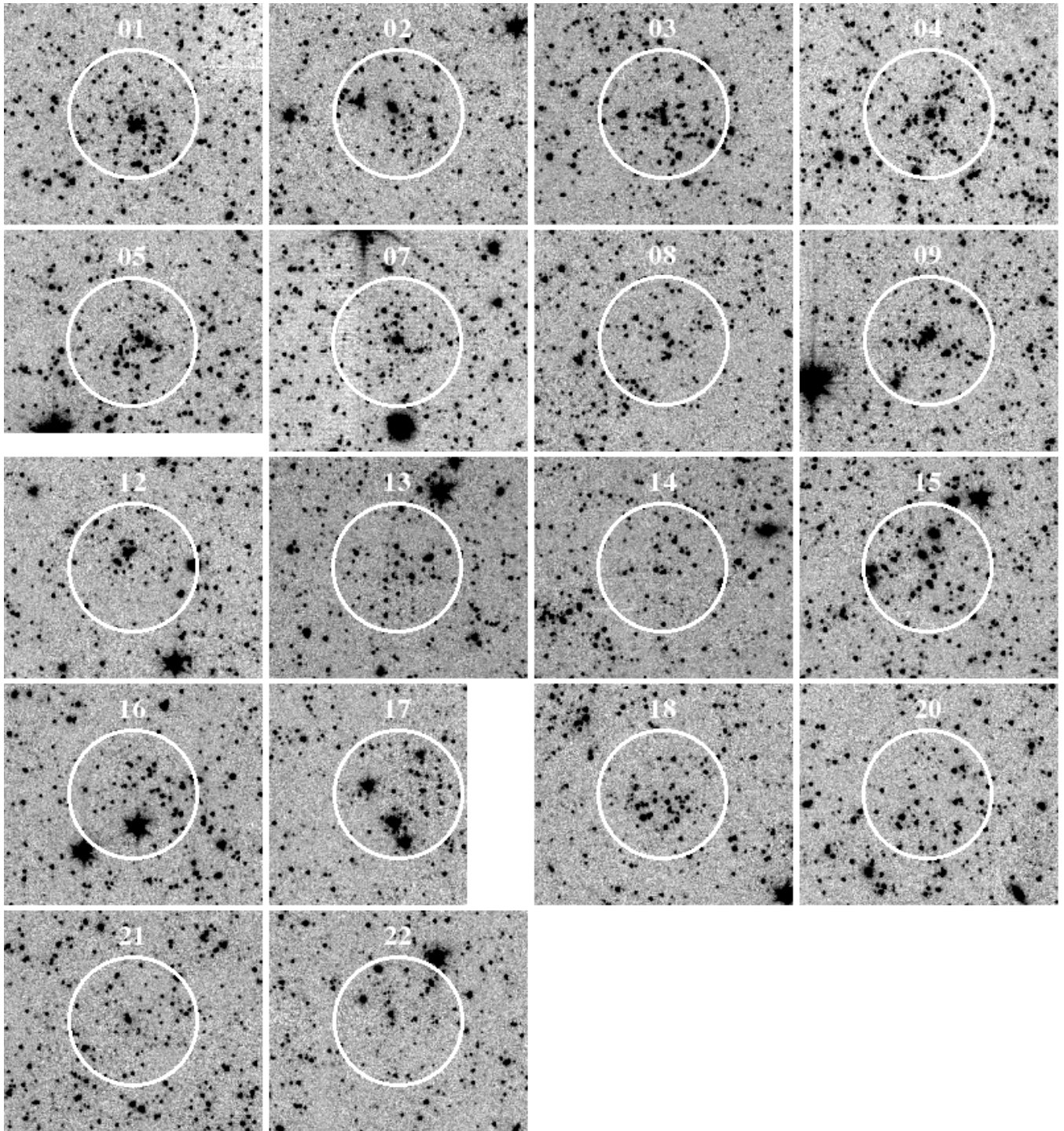


Figure 7. Spitzer/IRAC 3.6 μ m images of each cluster in the XMM-LSS sample. The white circle in each image displays the 1' circular aperture applied to each cluster. Each image is oriented north up and east left.

the BCG centroids in a manner consistent with a barycentre centroid error as discussed in Section 5.2.

When interpreting the stacked X-ray emission from each sub-sample, care must be taken to ensure that the resulting signal is dominated by extended ICM emission instead of the emission from weak AGN (strong AGN, i.e. those identified in individual exposures, having been masked prior to stacking). The stacked surface brightness distribution of each

SpARCS sub-sample is compared to a scaled point spread function (PSF) appropriate to the combined XMM detectors. Focussing on the BCG centroid stacks, panels *c/d/e* of Figures 14 and 15 indicate that extended X-ray emission is present in all three sub-samples. Following Anderson, Bregman & Dai (2013), we compute the X-ray hardness ratio as

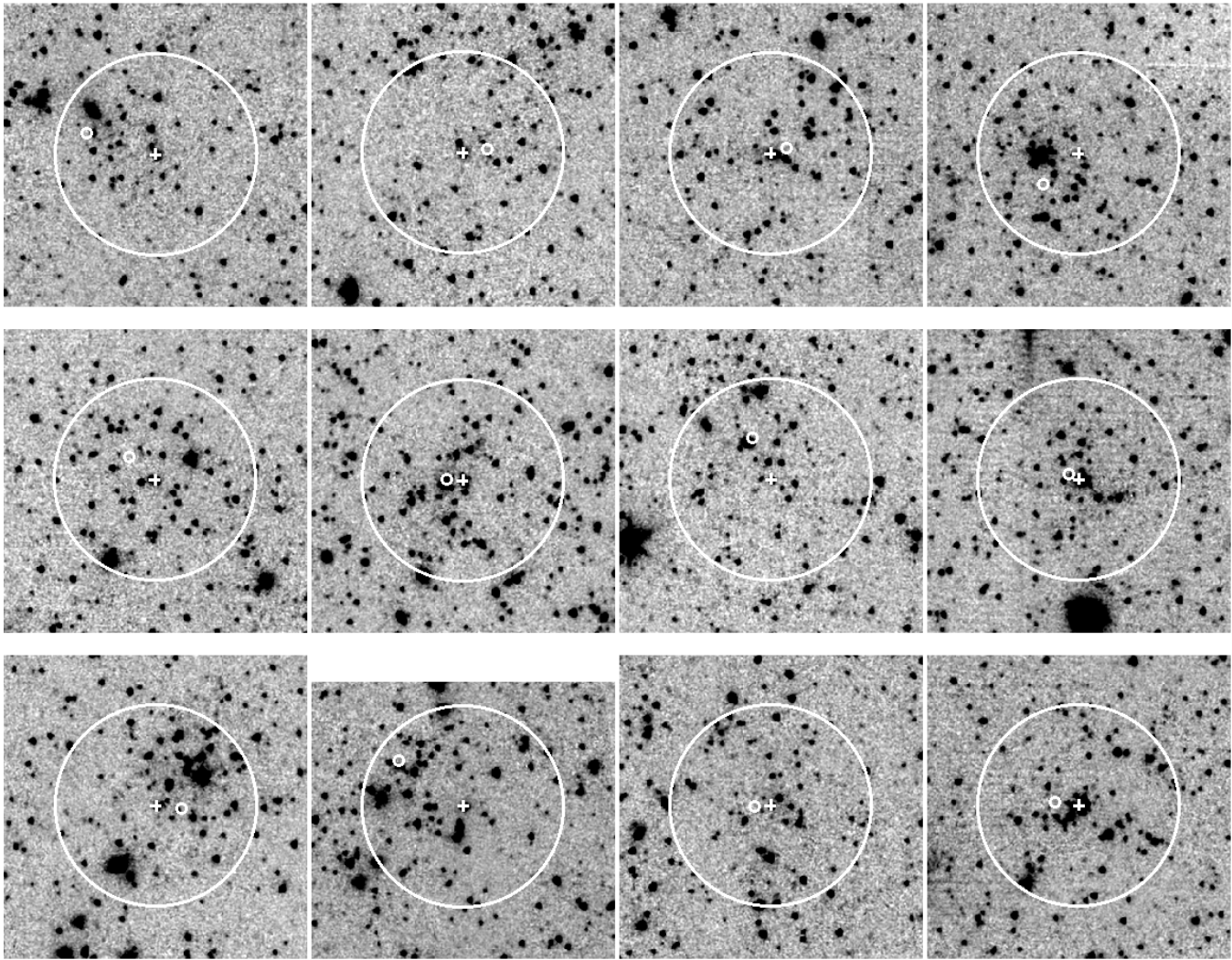


Figure 8. Spitzer/IRAC 3.6 μ m images of each cluster in the SpARCS X-ray bright sub-sample. The white circle in each image displays the 1' circular aperture applied to each cluster and is centered on the BCG position. The BCG and barycentre positions of each cluster are indicated respectively by the cross and the circle. Each image is oriented north up and east left.

$$HR = \frac{H - S}{H + S}, \quad (10)$$

within the central 15'' of each stack using the [0.5-2] keV and [2-10] keV intervals as the soft and hard band respectively. The results are plotted in Figure 16 and are compared to two, simple spectral models which respectively represent redshifted thermal ICM and non-thermal AGN emission (see caption for more details).

Given the simplicity of the model comparison it is perhaps appropriate only to comment that the XMM-LSS clusters, in addition to the SpARCS X-ray bright and X-ray faint, MIR bright sub-samples show little evidence for AGN contamination on the basis of hardness ratio. The hardness ratio for the stacked SpARCS X-ray faint, MIR faint sub-sample is nominally consistent with the simple AGN emission model presented here, albeit with large errors. However, the emission morphology in the stacked SpARCS X-ray faint, MIR faint sample is clearly extended, leaving the question of the fraction of BCGs in these clusters that host weak AGN relatively unconstrained. Webb et al. (2015) re-

port that 7/125 or 6% of SpARCS BCGs hosting bright 24 μ m sources – the majority of which occurring at $z \gtrsim 1$ – display IR colours consistent with being dominated by an AGN. Martini et al. (2013) report that the fraction of X-ray bright AGN hosted by cluster galaxies in 13 MIR-selected clusters at $1 < z < 1.5$ is 3%. It appears that, although weak emission from AGN associated with the BCG in each cluster may contribute to each stacked cluster X-ray image, the level of contamination, at a few percent, is unlikely to be large. In this sense we consider that the APEC thermal emission model employed to determine the k -correction used to convert between X-ray flux and luminosity (Section 5.1) remains reasonable.

Aperture flux and luminosity measurements were computed for the stacked X-ray images and comparable MIR aperture measurements were computed for each cluster sub-sample. Figure 17 displays the posterior probability distributions (PPDs) of each of the aperture fluxes and luminosities measured from each stacked image. Stacked aperture measures are plotted in Figure 2 and indicate significant

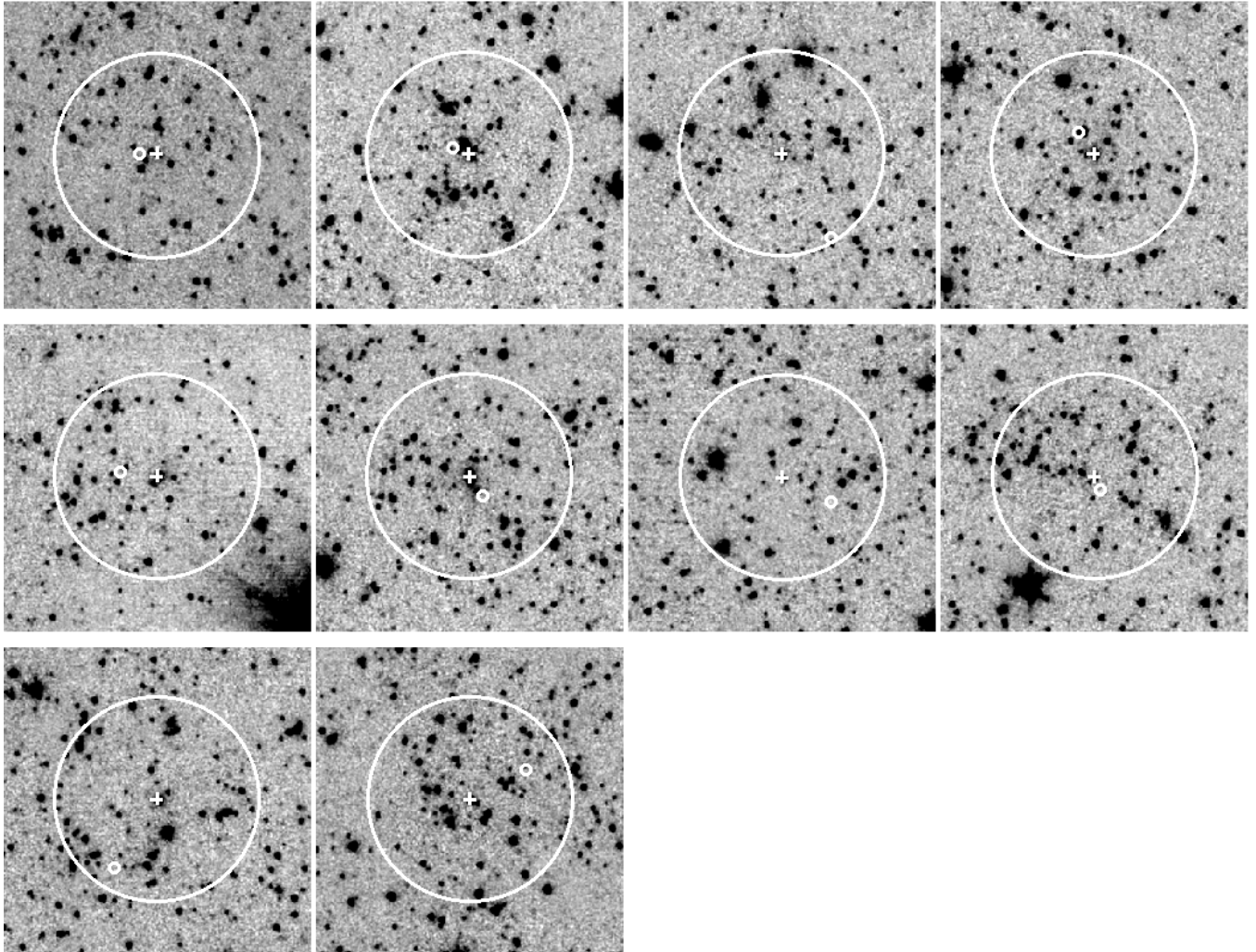


Figure 9. Spitzer/IRAC 3.6 μ m images of each cluster in the SpARCS X-ray faint, MIR bright sub-sample. The white circle in each image displays the 1' circular aperture applied to each cluster and is centered on the BCG position. The BCG and barycentre positions of each cluster are indicated respectively by the cross and the circle. Each image is oriented north up and east left.

detections for each sub-sample. Values corresponding to the stacked X-ray flux/luminosity represent the mode of the PPD and the error bars indicate the confidence interval enclosing 68% of the distribution. In particular, a significant (though faint) X-ray detection is obtained for the X-ray faint, MIR bright stack.

6 DISCUSSION AND CONCLUSIONS

The comparison of the properties of the XMM-LSS and SpARCS distant cluster samples has revealed that X-ray bright clusters, whether detected using X-ray or optical-MIR methods, display very similar MIR and X-ray surface brightness distributions. We note however, that there is tentative evidence that such X-ray bright clusters detected using optical-MIR methods display numerically larger populations of red sequence galaxies than X-ray selected counterparts, an observation consistent with SpARCS selection based upon the presence of an identifiable red sequence.

There are further physical differences between cluster

samples detected using each method. Within the optical-MIR selected SpARCS sample we have identified three sub-samples of clusters based upon their X-ray and MIR aperture flux measurements. In particular, the sub-sample of X-ray faint, MIR bright SpARCS clusters display the same redshift distribution as X-ray bright SpARCS clusters yet show, on-average, higher values of the BCG-barycentre distance. In the literature, larger values of BCG-cluster centroid offset have been demonstrated to be strongly correlated with more shallow X-ray surface brightness profiles (e.g. Sanderson, Edge & Smith 2009; Mantz et al. 2015).

Interpreting greater values of the BCG-centroid distance as an indicator of dynamical disturbance in a cluster might provide an explanation of their relatively low X-ray compared to stellar emission, e.g. if the X-ray emitting gas has been disturbed by a recent merger, reducing the X-ray surface brightness as a result (e.g. Eckert, Molendi & Palatani 2011; Barnes et al. 2017). An alternative explanation is that the X-ray faint, MIR bright cluster sub-sample is associated with secular mass assembly in massive structures whereby a compact, low-mass, virialised core is surrounded

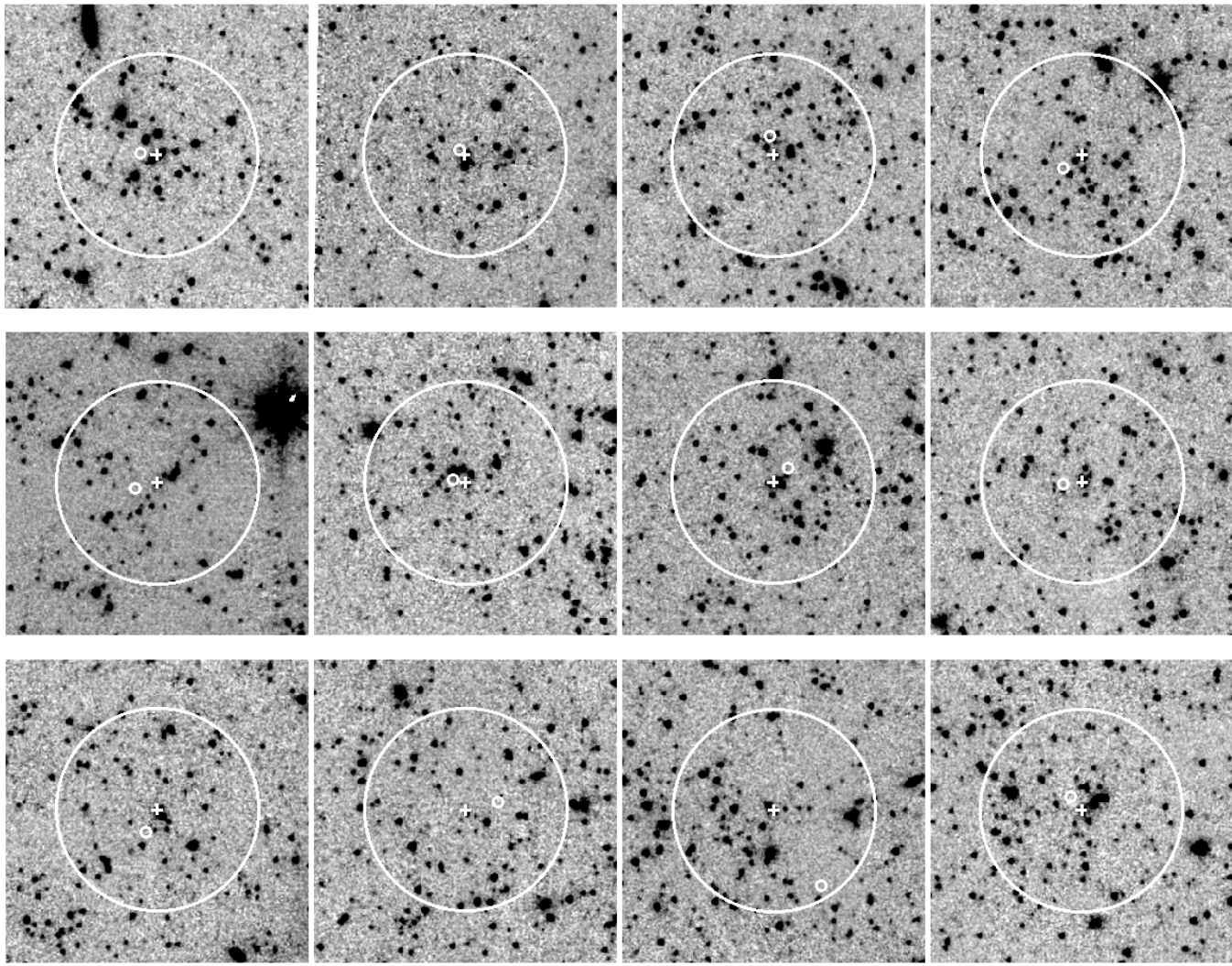


Figure 10. Spitzer/IRAC 3.6 μ m images of a subset of clusters from the SpARCS X-ray faint, MIR faint sub-sample. The top, middle and bottom rows show typical clusters at low, middle and high redshift within this sub-sample. The white circle in each image displays the 1' circular aperture applied to each cluster and is centered on the BCG position. The BCG and barycentre positions of each cluster are indicated respectively by the cross and the circle. Each image is oriented north up and east left.

by an envelope of accreting material (c.f. Figure 1 of Muldrew, Hatch & Cooke 2015). The location of the BCG can be perturbed but, overall, the mass accretion is on-going and continuous as opposed to associated with large, stochastic merger events. Note that this statement regarding the dynamical state of optical-MIR selected clusters does not ignore the observation that X-ray selected clusters also display a range of relaxation states (e.g. Sanderson, Edge & Smith 2009; Lavoie et al. 2016). However, the departures from relaxation are slight compared to that observed in the present SpARCS sample.

A contrasting argument, that such X-ray faint, MIR bright systems represent projected large-scale structure variations along the line-of-sight, as opposed to bound systems displaying incomplete virialisation, requires a rate of contamination in marked disagreement with previously determined rates of false detection in such systems (Gladders & Yee 2000) and with the successful results of spectroscopic follow-up campaigns employing these clusters (e.g.

Muzzin et al. 2012). Of the $z > 0.8$ SpARCS clusters with IRAC1 aperture fluxes $> 650\mu\text{Jy}$, 8/10 are X-ray faint. The corresponding value for clusters with aperture luminosities $L_K > 2.5 \times 10^{13}L_\odot$ is 8/16.

The analysis presented in this paper shares many similarities with that of Rossetti et al. (2017) who compare clusters selected from the Planck SZ catalogue with X-ray selected clusters from the MAssive Cluster Survey (MACS; Ebeling et al. 2010). Rossetti et al. (2017) demonstrate that the X-ray cool-core fraction of SZ detected clusters is significantly lower than that determined for X-ray selected clusters and claim that this result can be explained in large part as due to the relative detectability of clusters of varying surface brightness properties in each sample. Interestingly, they also detect a population of shallow surface brightness profile (NCC) SZ “bright” clusters that are undetected in MACS yet possess X-ray luminosities based upon an extrapolated $L_X - Y$ relation that nominally place them within the MACS

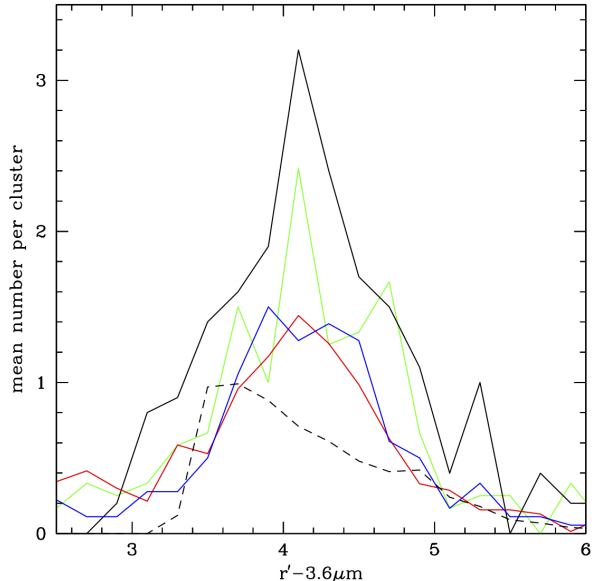


Figure 11. Average $r' - 3.6\mu\text{m}$ colour histogram for clusters in each sub-sample: XMM-LSS (blue), X-ray bright SpARCS (green), X-ray faint, MIR faint SpARCS (red), X-ray faint, MIR bright (black). The dashed black line shows the scaled colour histogram generated by placing 100 $1'$ apertures at random within the survey area and extracting all sources satisfying the distant galaxy colour cut. Only sources satisfying $[3.6\mu\text{m}] < 21$ when corrected to $z = 1$ are displayed. No k - or distance modulus corrections are applied to the randomly collected source photometry.

selection criteria (Figure 9 of Rossetti et al. 2017), i.e. X-ray under luminous for their SZ-determined mass.

X-ray emission in the X-ray faint, MIR bright sub-sample of SpARCS clusters is clearly present and associated with the location of the BCG in each cluster. Figures 14 and 15 indicate that the stacked X-ray surface brightness distribution in these clusters is similar in shape to X-ray bright clusters yet offset to lower overall normalisation. This would appear to support the assertion that X-ray faint, MIR bright SpARCS clusters represent bona-fide clusters where a low-mass, virialised core surrounded by an extended, bound envelope of material.

This conclusion is also supported by the observation that all samples of clusters considered in this paper display identifiable red sequence galaxy populations, thus confirming that we are observing real galaxy overdensities of common age and star formation history as opposed to chance projections. If low mass groups are indeed the sites of pre-processing to create such red sequence populations (e.g. Li, Yee & Ellingson 2009) then these structures, accreting onto X-ray faint, MIR bright SpARCS clusters may be respon-

sible for the high values of MIR aperture fluxes and luminosities observed in these systems. In addition, there is tentative evidence that the red sequence population of X-ray selected clusters is marginally smaller than the red sequence in optical-MIR selected clusters of comparable X-ray brightness (c.f. Donahue et al. 2002). However, the precision achievable in this current study does not permit more than a tentative statement.

It should also be noted that all of the above conclusions are based upon the average properties of sub-samples of clusters and thus any information of the distribution of relaxation states of optical-MIR selected clusters is not available. What we can say however, based upon the distribution of clusters in the X-ray versus MIR aperture flux plane, is that each SpARCS sub-sample is not isolated from any other; instead each is drawn from a continuous range of properties formed by the overall SpARCS sample and each is identified using sensible, yet essentially arbitrary, cuts.

Furthermore, if the X-ray faint, MIR bright sub-sample of clusters is indeed associated with either ongoing mass assembly onto a virialised core or disruption from a recent major merger, then the X-ray surface brightness profiles of such clusters would be expected to change significantly as they evolve to a more relaxed state. The surface brightness profile determines the detectability of faint clusters and therefore modelling of X-ray cluster surface brightness profiles (or equivalently the astrophysics underlying the surface brightness profile) is a key factor in computing an accurate cluster selection function. This point extends beyond the inclusion of an explicit surface brightness expression for clusters in the selection modelling (e.g. Pacaud et al. 2006) to a description that includes a distribution of surface brightness properties informed by the dynamical state of the cluster population. Cluster mass assembly state therefore represents an important source of astrophysical uncertainty, particularly in the application of X-ray selected cluster samples to cosmological analyses employing cluster number counts (e.g. Borgani et al. 2001; Mantz et al. 2008).

If the dynamical state of galaxy clusters is indeed causing surface brightness driven incompleteness in observations of galaxy clusters, how should such observations be reconciled with the aim of using galaxy clusters as a probe of the cosmological model? For cosmological applications, one typically compares the observed sample to the true population as provided by either a numerical model or simulations.

Focussing on the relationship between mass growth in galaxy clusters and their observability as a function of wavelength, if the X-ray under luminous structures identified in this paper are collapsing filaments, would they pass applied friends-of-friends or spherical overdensity criteria to qualify as a halo and therefore contribute to the mass function (e.g. Watson et al. 2013)? If yes, then X-ray selection functions might require an additional incompleteness term (e.g. a sub-population of X-ray dark haloes in the scaling relation model). If no, then optical-IR samples might require an additional contamination term (e.g. to represent the selection of bound yet unvirialised structures). If X-ray under luminous clusters instead represent recent mergers that have not yet reached equilibrium, one might consider whether deblending methods are consistent between observations and simulations. Would numerical simulations identify one or two

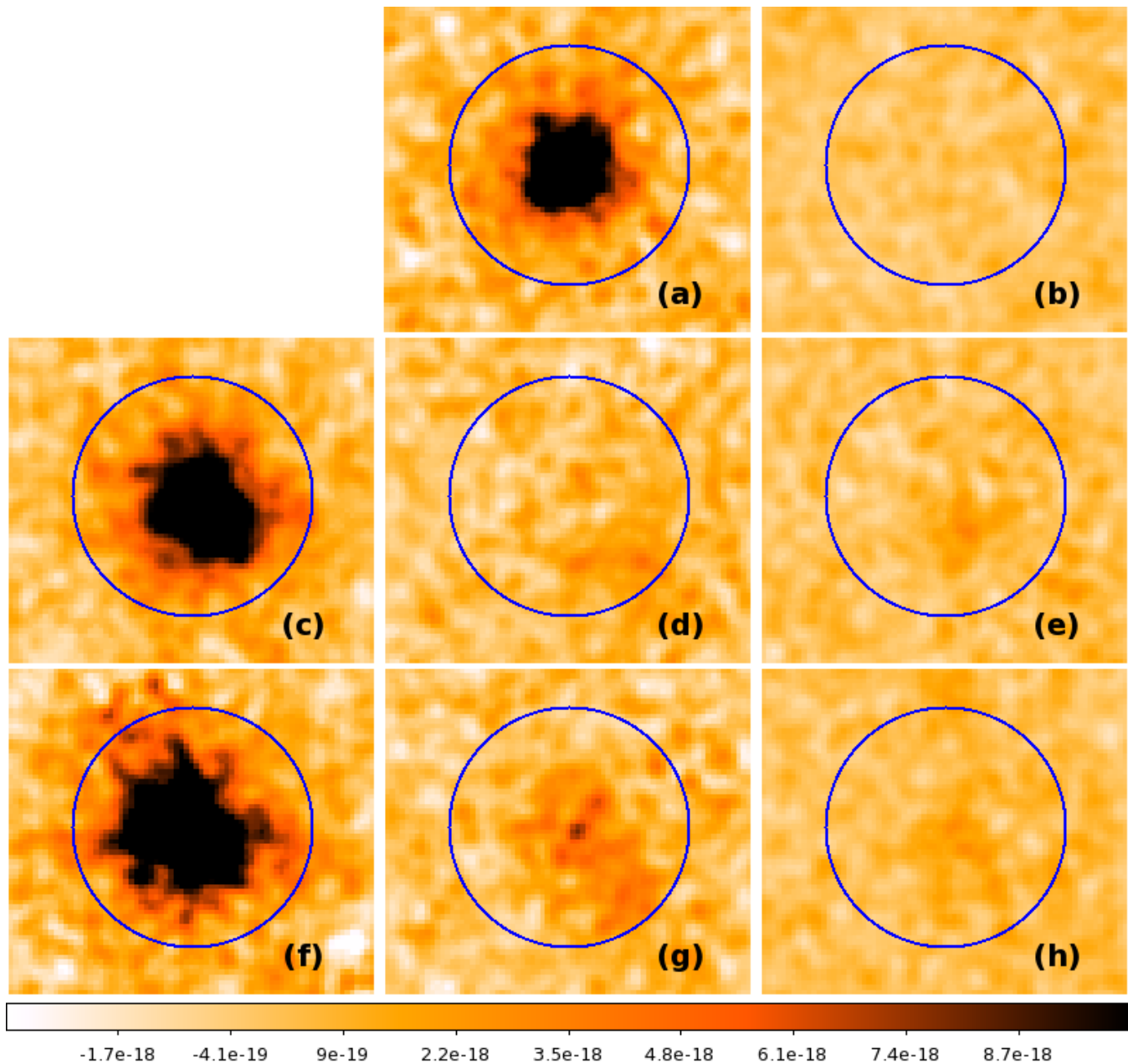


Figure 12. Stacked X-ray flux images for each cluster sub-sample. Each image is smoothed with a Gaussian kernel of sigma equal to three pixels. The scale bar indicates the flux per pixel in units of $\text{ergs s}^{-1} \text{cm}^{-2}$. Panels: a) XMM-LSS clusters, b) Stack of 100 random positions, c,d,e) SpARCS clusters stacked on the catalogue barycentre position, c) X-ray bright, d) X-ray faint, MIR bright, e) X-ray faint, MIR faint, f,g,h) SpARCS clusters stacked on the catalogue BCG position, f) X-ray bright, g) X-ray faint, MIR bright, h) X-ray faint, MIR faint. The blue circle in each panel represents the $1'$ radius aperture used to measure individual cluster X-ray fluxes.

halos? Would X-ray image analysis do so, for example, were deeper data available?

A related question is whether this X-ray under luminous population is represented within scaling relation models. Do such systems represent simply the low-end of the log-normal distribution derived from analysis of X-ray samples, or are they instead a population so far relatively undetected by X-ray selected cluster studies? If they are undetected, this would support the idea that X-ray scaling relations should be derived from cluster samples selected at other wavelengths e.g. Andreon et al. (2016).

In closing, it is clear that any survey for galaxy clusters provides only a partial view of the true population of virial structures above a given mass threshold. However, comparisons of cluster samples compiled at multiple wavelengths, such as performed in this paper and others, provide a means to reveal the nature and extent of any bias. Ultimately, and possibly with recourse to simulated clusters samples incorporating both cosmological and gas physics (e.g. McCarthy et al. 2017; Barnes et al. 2017), the effects of such bias can be corrected for and an impartial view obtained of the for-

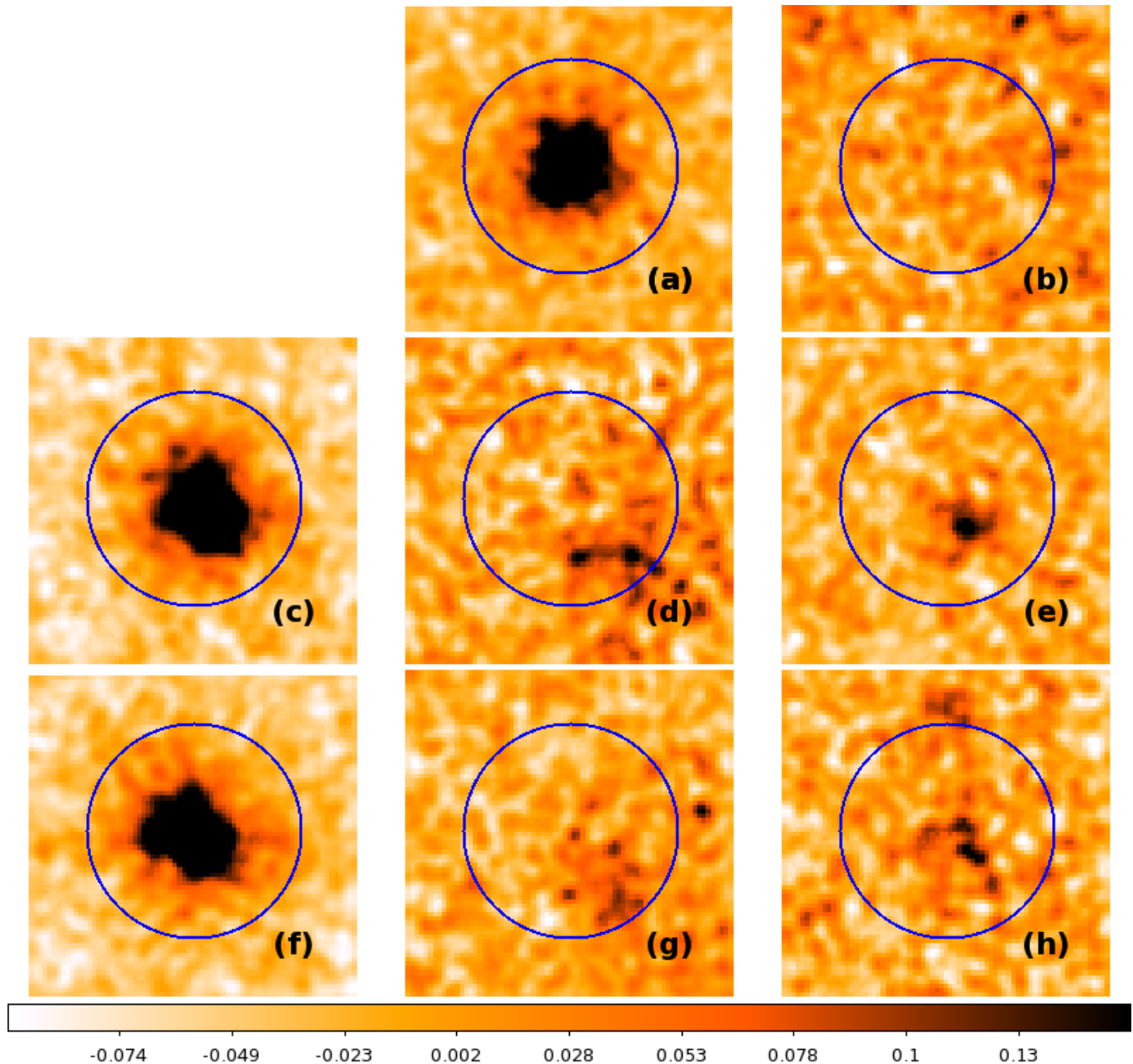


Figure 13. Stacked X-ray luminosity images for each cluster sub-sample. The caption information is the same as for Figure 12 with the exception that the scale bar indicates the luminosity per pixel in units of 10^{41} ergs s^{-1} .

mation of large scale structure and the evolution of galaxies therein.

ACKNOWLEDGMENTS

The authors would like to thank the anonymous referee for their comments that resulted in many improvements in the paper. The authors further wish to thank Dr. Irene Pintos Castro for checking our XMM-SpARCS matching results. MERC acknowledges support by the Bonn-Cologne Graduate School of Physics and Astronomy (BCGS) and the German Aerospace Agency (DLR) with funds from the Ministry of Economy and Technology (BMWi) through grant 50

OR 1608. G.W. acknowledges financial support for this work from NSF grant AST-1517863 and from NASA through programs GO-13306, GO-13677, GO-13747 & GO-13845/14327 from the Space Telescope Science Institute, which is operated by AURA, Inc., under NASA contract NAS 5-26555, and grant number 80NSSC17K0019 issued through the Astrophysics Data Analysis Program (ADAP).

REFERENCES

- Alberts S. et al., 2016, *ApJ*, 825, 72
 Anderson M. E., Bregman J. N., Dai X., 2013, *ApJ*, 762, 106

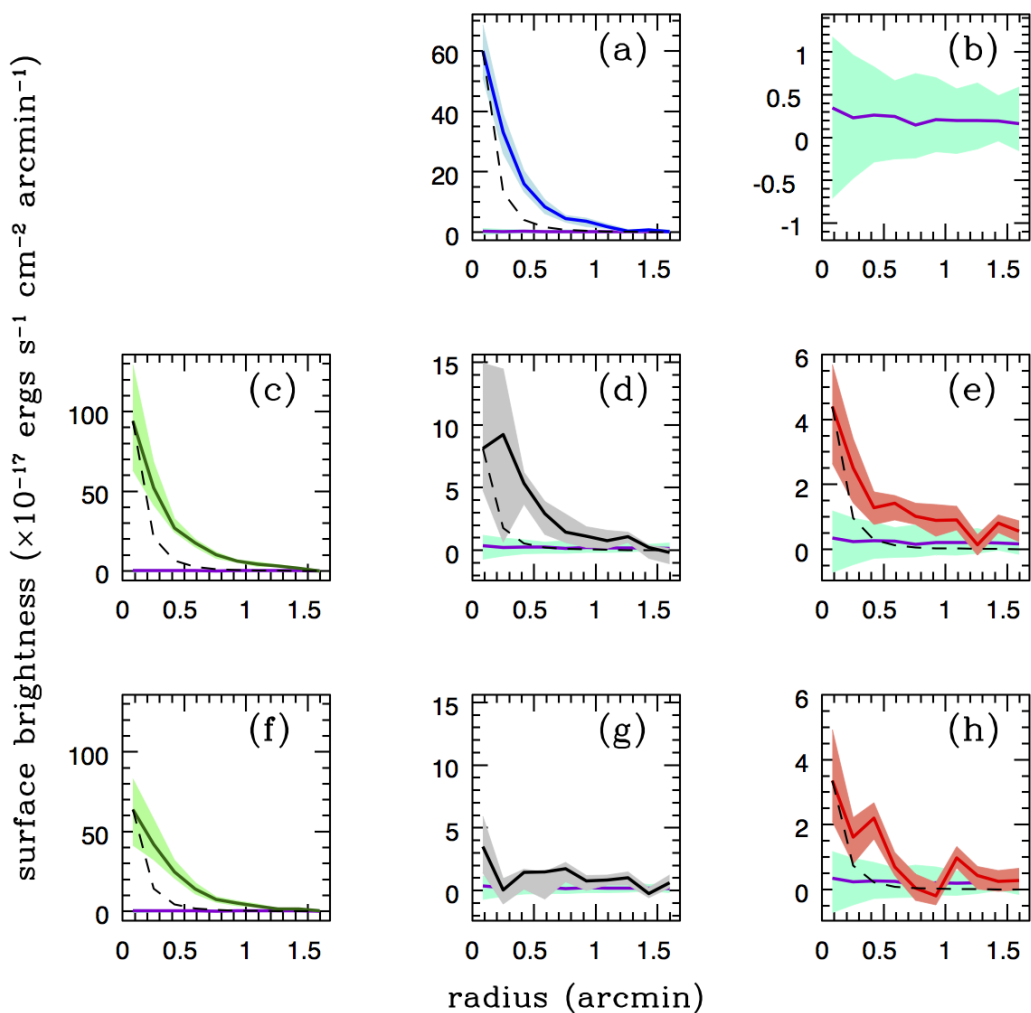


Figure 14. The differential angular X-ray surface brightness distribution in flux of each stacked cluster sub-sample. The ordering of the panels follows that of Figure 12. The shaded area about each solid line represents the 68% confidence interval obtained from 1000 bootstrap realisations of each stack. Where shown, the black dashed line indicated the XMM PSF scaled to the central surface brightness.

Anderson M. E., Gaspari M., White S. D. M., Wang W., Dai X., 2015, MNRAS, 449, 3806

Andreon S., Serra A. L., Moretti A., Trinchieri G., 2016, A&A, 585, A147

Arnaud K. A., 1996, in Astronomical Society of the Pacific

Conference Series, Vol. 101, Astronomical Data Analysis Software and Systems V, Jacoby G. H., Barnes J., eds., p. 17

Barkhouse W. A. et al., 2006, ApJ, 645, 955

Barnes D. J., Kay S. T., Henson M. A., McCarthy I. G.,

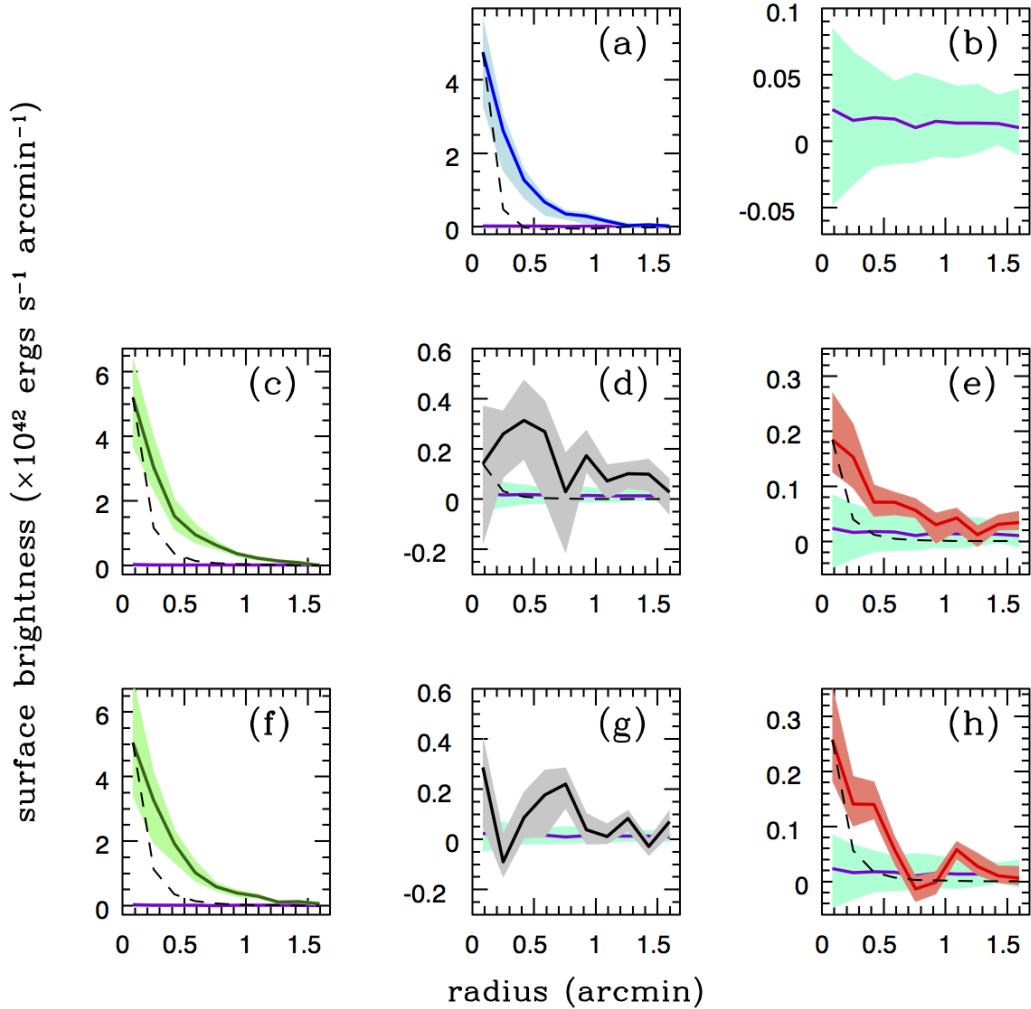


Figure 15. The differential angular X-ray surface brightness distribution in luminosity of each stacked cluster sub-sample. The caption information is the same as for Figure 14.

Schaye J., Jenkins A., 2017, *MNRAS*, 465, 213
 Bayliss M. B. et al., 2014, *ApJ*, 794, 12
 Bergé J. et al., 2008, *MNRAS*, 385, 695
 Böhringer H. et al., 2001, *A&A*, 369, 826
 Borgani S. et al., 2001, *ApJ*, 561, 13
 Brodwin M. et al., 2013, *ApJ*, 779, 138

Bruzual G., Charlot S., 2003, *MNRAS*, 344, 1000
 Chiappetti L. et al., 2013, *MNRAS*, 429, 1652
 Clerc N., Sadibekova T., Pierre M., Pcaud F., Le Fèvre J.-P., Adami C., Altieri B., Valtchanov I., 2012, *MNRAS*, 423, 3561
 De Propriis R., Stanford S. A., Eisenhardt P. R., Holden

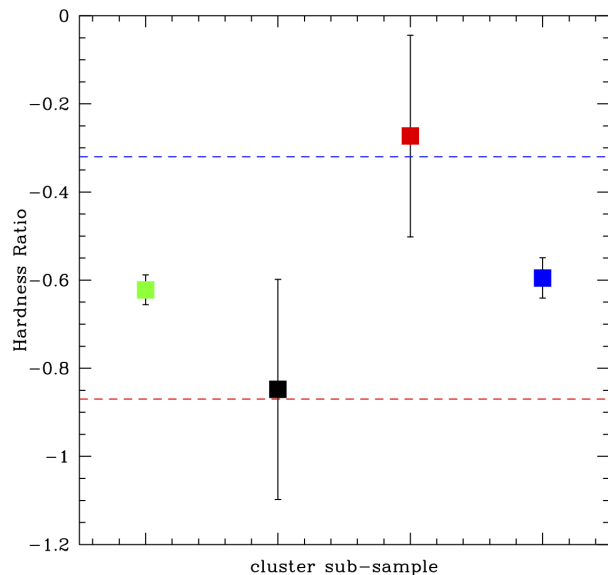


Figure 16. Hardness ratios computed for each cluster sub-sample: XMM-LSS (blue), X-ray bright SpARCS (green), X-ray faint, MIR faint SpARCS (red), X-ray faint, MIR bright SpARCS (black). One sigma errors on the HR are calculated using a Monte Carlo simulation employing posterior probability distribution functions of count-rate within the $15''$ aperture. The red dashed line indicates the HR expected from thermal emission, in this case an absorbed APEC model with $T = 2$ considered at $z = 1$. The blue dashed line indicates the HR expected from a simple model of AGN emission, i.e. an absorbed power law with index of -2, again considered at $z = 1$.

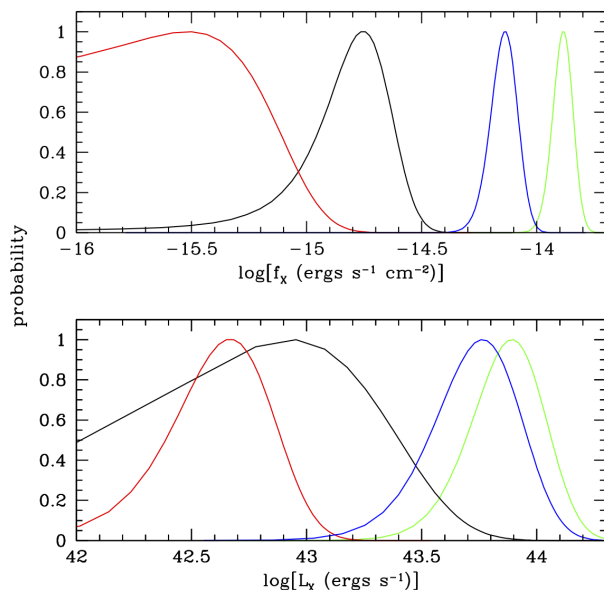


Figure 17. Posterior probability distributions for aperture flux and luminosity measured from the stacked X-ray images: XMM-LSS (blue), X-ray bright SpARCS (green), X-ray faint, MIR faint SpARCS (red), X-ray faint, MIR bright SpARCS (black).

B. P., Rosati P., 2007, AJ, 133, 2209
 Donahue M. et al., 2002, ApJ, 569, 689
 Ebeling H., Edge A. C., Mantz A., Barrett E., Henry J. P., Ma C. J., van Speybroeck L., 2010, MNRAS, 407, 83
 Eckert D., Molendi S., Paltani S., 2011, A&A, 526, A79
 Ehlert S. et al., 2015, MNRAS, 446, 2709
 Foltz R. et al., 2015, ApJ, 812, 138
 Galametz A. et al., 2009, ApJ, 694, 1309
 Gavazzi R., Soucail G., 2007, A&A, 462, 459
 Gilbank D. G. et al., 2018, MNRAS, submitted
 Gilbank D. G., Bower R. G., Castander F. J., Ziegler B. L., 2004, MNRAS, 348, 551
 Gioia I. M., Maccacaro T., Schild R. E., Wolter A., Stocke J. T., Morris S. L., Henry J. P., 1990, ApJS, 72, 567
 Gladders M. D., Yee H. K. C., 2000, AJ, 120, 2148
 Gwyn S. D. J., 2012, AJ, 143, 38
 Hayashi M., Kodama T., Koyama Y., Tadaki K.-I., Tanaka I., 2011, MNRAS, 415, 2670
 Jimeno P., Broadhurst T., Lazkoz R., Angulo R., Diego J.-M., Umetsu K., Chu M.-c., 2017, MNRAS, 466, 2658

Kaiser N., 1986, MNRAS, 222, 323
 Kron R. G., 1980, ApJS, 43, 305
 Lavoie S. et al., 2016, MNRAS, 462, 4141
 Li I. H., Yee H. K. C., Ellingson E., 2009, ApJ, 698, 83
 Lin Y.-T., Mohr J. J., Stanford S. A., 2004, ApJ, 610, 745
 Lonsdale C. J. et al., 2003, PASP, 115, 897
 Lotz J. M. et al., 2013, ApJ, 773, 154
 Mahdavi A., Geller M. J., 2001, ApJ, 554, L129
 Mantz A., Allen S. W., Ebeling H., Rapetti D., 2008, MNRAS, 387, 1179
 Mantz A. B., Allen S. W., Morris R. G., Schmidt R. W., von der Linden A., Urban O., 2015, MNRAS, 449, 199
 Marriage T. A. et al., 2011, ApJ, 737, 61
 Martini P. et al., 2013, ApJ, 768, 1
 McCarthy I. G., Schaye J., Bird S., Le Brun A. M. C., 2017, MNRAS, 465, 2936
 McDonald M. et al., 2012, Nature, 488, 349
 Menanteau F. et al., 2012, ApJ, 748, 7
 Miyazaki S. et al., 2002, ApJ, 580, L97
 Muldrew S. I., Hatch N. A., Cooke E. A., 2015, MNRAS, 452, 2528
 Muzzin A., Wilson G., Lacy M., Yee H. K. C., Stanford S. A., 2008, ApJ, 686, 966
 Muzzin A. et al., 2012, ApJ, 746, 188
 Muzzin A. et al., 2009, ApJ, 698, 1934
 Nantais J. B. et al., 2017, MNRAS, 465, L104

- Nantais J. B. et al., 2016, *A&A*, 592, A161
Nastasi A. et al., 2011, *A&A*, 532, L6
Oguri M. et al., 2017, ArXiv e-prints
Pacaud F. et al., 2006, *MNRAS*, 372, 578
Park T., Kashyap V. L., Siemiginowska A., van Dyk D. A., Zezas A., Heinke C., Wargelin B. J., 2006, *ApJ*, 652, 610
Pierre M. et al., 2004, *JCAP*, 9, 11
Planck Collaboration et al., 2014, *A&A*, 571, A20
Postman M., Lubin L. M., Gunn J. E., Oke J. B., Hoessel J. G., Schneider D. P., Christensen J. A., 1996, *AJ*, 111, 615
Reichardt C. L. et al., 2013, *ApJ*, 763, 127
Rossetti M., Gastaldello F., Eckert D., Della Torre M., Pantiri G., Cazzoletti P., Molendi S., 2017, *MNRAS*, 468, 1917
Rozo E., Bartlett J. G., Evrard A. E., Rykoff E. S., 2014, *MNRAS*, 438, 78
Rozo E., Rykoff E. S., 2014, *ApJ*, 783, 80
Rozo E. et al., 2010, *ApJ*, 708, 645
Rykoff E. S. et al., 2014, *ApJ*, 785, 104
Sadibekova T., Pierre M., Clerc N., Faccioli L., Gastaud R., Le Fevre J.-P., Rozo E., Rykoff E., 2014, *A&A*, 571, A87
Sanderson A. J. R., Edge A. C., Smith G. P., 2009, *MNRAS*, 398, 1698
Sarazin C. L., 1986, *Reviews of Modern Physics*, 58, 1
Staniszewski Z. et al., 2009, *ApJ*, 701, 32
Starikova S. et al., 2014, *ApJ*, 786, 125
van der Burg R. F. J., Muzzin A., Hoekstra H., Wilson G., Lidman C., Yee H. K. C., 2014, *A&A*, 561, A79
van Dyk D. A., Connors A., Kashyap V. L., Siemiginowska A., 2001, *ApJ*, 548, 224
Watson W. A., Iliev I. T., D'Aloisio A., Knebe A., Shapiro P. R., Yepes G., 2013, *MNRAS*, 433, 1230
Webb T. M. A. et al., 2015, *ApJ*, 814, 96
Willis J. P. et al., 2013, *MNRAS*, 430, 134
Wilson G. et al., 2009, *ApJ*, 698, 1943
Wittman D., Dell'Antonio I. P., Hughes J. P., Margoniner V. E., Tyson J. A., Cohen J. G., Norman D., 2006, *ApJ*, 643, 128

This paper has been typeset from a \TeX / \LaTeX file prepared by the author.